Experimental Investigation of Mode II Fracture and Fatigue in Unidirectional Carbon/Epoxy Composite Beams

Ryan Howe

A thesis
submitted in partial fulfillment of the
requirements for the degree of

Master of Science in Aeronautics & Astronautics

University of Washington

2021

Committee:

Marco Salviato

Richard Wiebe

Program Authorized to Offer Degree:
Aeronautics & Astronautics

University of Washington

Abstract

Experimental Investigation of Mode II Fracture and Fatigue in Unidirectional Carbon/Epoxy Composite Beams

Ryan Howe

Chair of the Supervisory Committee:
Assistant Professor Marco Salviato
Department of Aeronautics & Astronautics

This paper investigates mode II quasi-brittle fracture and fatigue in laminated composite structures and characterizes the phenomena in the form of size effect and Cohesive Zone Models (CZMs). This research focuses primarily on mode II quasi-static fracture, but also includes a preliminary experimental investigation of quasi-static fatigue and numerical investigation of forced-dynamic fatigue.

For these case studies, composite beam specimens were manufactured in-house using a closed-molding process to create End-Notched Flexure (ENF) test specimens of different sizes, using Toray T700G and T800S carbon/epoxy prepregs. An initial pre-crack was induced using a Teflon insert at the midplane of each specimen, with predetermined crack lengths. Each case aimed to study crack crowth via fracture or fatigue using geometrically scaled sizes to study the size effect phenomena. For the quasi-static fracture case, an additional analysis was applied to identify the influence of Teflon thickness on the fracture energy using two Teflon films with thicknesses of 76 μm and 12.5 μm, respectively. Experimental data was obtained through ENF tests following American Society for Testing and Materials (ASTM) D7905 parameters, while utilizing microscopic 2D and full-field 3D Digital Image Correlation (DIC) technology to obtain both local and global behavior of the beams.

The fracture energy for each Teflon case was analyzed using both Linear Elastic Fracture Mechanics (LEFM) and Bažant's Type II Size Effect Law (SEL). It was found that using

LEFM resulted in different values for differing scaled geometric specimen sizes, contradicting fracture energy as a material property. To address this issue, Bažant's Type II SEL was applied to the experimental data which produced a single value for fracture energy as a material property. The impact of Teflon size was also observed under this analysis. It was found the thick Teflon, 76 μm, created a larger resin pocket in the front of the crack tip, causing a more complex stress profile at the crack tip. Thus, a larger fracture energy was predicted for the thick insert case by size effect analysis.

From these experimental results, a CZM was formulated based on the 12.5 μm thin Teflon case. This removed the impact of the resin pocket and complex stress distribution found with the 76 μm Teflon insert. The CZM parameters were characterized based on microscopic DIC data of the crack tip region obtained from the small size fracture testing. The 3D DIC data was used for validation of global behavior simulated using the CZM, while the experimental result of the thick Teflon insert case provided an additional data set for robust validation of the CZM. The results of this investigation suggest a piece-wise CZM shape to account for the size effect influence.

A preliminary experimental quasi-static fatigue investigation was also conducted using displacement controlled tests on size affected specimens. The results of these fatigue tests enabled the formulation of the threshold and stable crack growth regions of the fatigue Paris Curve for three different specimen sizes. This identified increasing values for threshold Stress Intensity Factors, K_{th}, and increasing slopes for the linear fatigue crack growth for increasing specimen size, further demonstrating the size effect influence. Future work is outlined to develop all regions of the fatigue Paris Curve using both displacement and load controlled testing methods.

TABLE OF CONTENTS

Page

LIST OF FIGURES

LIST OF TABLES

ACRONYMS

AFB Air Force Base

AFRL Air Force Research Lab

ASTM American Society for Testing and Materials

CZM Cohesive Zone Model

DCB Double-Cantilever Beam

DIC Digital Image Correlation

ENF End-Notched Flexure

FEA Finite Element Analysis

FEM Finite Element Model

FPZ Fracture Process Zone

GUI Graphic User Interface

JIS Japanese Industrial Standard

LEFM Linear Elastic Fracture Mechanics

NPC Non-Precracked

PC Precracked

PTFE Polytetrafluoroethylene

SEL Size Effect Law

SEM Scanning Election Microscope

SENB Single End-Notched Bending

UD Uni-Directional

UW University of Washington

ACKNOWLEDGMENTS

I would like to acknowledge my professors, Professor Salviato and Professor Wiebe for their guidance and support during this project. Without them, I would not have had the opportunity to work on such a hands-on project allowing me a wide variety of experience at UW.

A special thanks to Shiva Goutham Pattapu for his help and teaching in this research. He shared his invaluable expertise (and friendship) during my first year at UW making the transition to working on this project much easier.

Another thanks to Han-Gyu Kim for his mentorship and knowledge throughout the project. Han-Gyu invested a lot of time in me to improve my learning in this research and the Master's degree, in general. He was always available to answer any questions I had - without his help and mastery of these subjects, I would not have the necessary knowledge to complete this degree.

Thanks to the Air Force and AFRL for sponsoring my degree and allowing me to live the dream first assignment. I will draw on my Seattle experiences to improve my officership and be a better leader as a result.

Lastly, thanks to my friends and family for supporting me all the way through. These relationships make a great experience that much better. Could not have done it without you!

Chapter 1

INTRODUCTION

1.1 Brief Description of Carbon Fiber

Carbon composites are becoming increasingly employed in many different industries, including civil, automotive, aerospace, and many more [1]. This is largely due to the performance benefits over traditional materials, with higher strength-to-weight ratios, corrosion resistance, fatigue life, and ease of design-ability. Carbon fiber structures can be molded and laid up to provide advantageous qualities under different loading scenarios which are unable to be achieved by traditional, isotropic material. Manufactured by laying various carbon plies combined with epoxy resin, complex designs can be achieved much easier than machine-able metals which are now being substituted for carbon fiber parts. Because of these positive attributes, composite materials are becoming more commonplace in structures than ever before.

1.2 Current Uses in Aerospace and Air Force Industries

Aircraft and aerospace industries unsurprisingly benefit from stronger and lighter material. For many aircraft, weight savings translates to fuel savings, better payload capacity, and higher performance and range capabilities [1]. For these reasons and those aforementioned, the Air Force and other aerospace industries are beginning to employ this material on a deployable scale. Famously used by aircraft such as the B-2 Stealth Bomber and the F-22 Raptor, these stiff, lightweight materials have enabled a level of air superiority unmatched in history [2].

Further development of composite materials has aircraft ranging from the newest 5th generation fighter, the F-35, to civilian industries with Boeing's 787 using 35% and 50% composite material, by weight respectively [5, 6]. With the success of this material in standard aircraft, carbon composites are being extensively introduced in faster and more agile aircraft

(a) US Air Force F-22 stealth fighter, using mainstream composite materials [3]

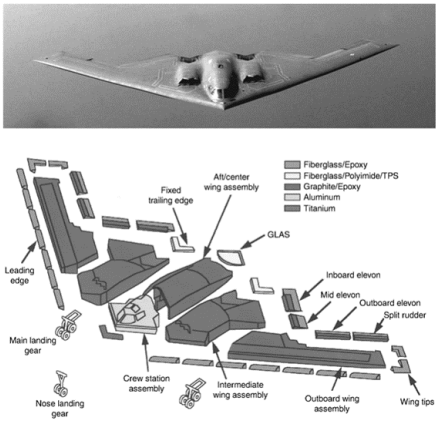

(b) US Air Force B-2 stealth bomber showing material components in manufacturing [4]

Figure 1.1: Air Force aircraft employing composite materials

such as hypersonic flight vehicles, which impose greater stresses on the material than seen in typical subsonic, and even supersonic flight regimes [7]. Due to the aero-thermal-structural coupling of aircraft, the materials of hypersonic flight vehicles can experience thermal or mechanical buckling, causing dynamic snap-through and increase damage propagation and delamination at a faster rate [8].

1.3 Theoretical Background

Nonlinear material behavior that occurs due to in-flight loading can cause high stresses and large deformations within the structures. Specifically, periodic dynamic snap-through can lead to catastrophic low-cycle fatigue failure due to the amplification of stresses under these conditions [8]. Material response and failure due to these in-flight loads are often more affected by mode II, shearing and delamination failure, than the more commonly tested, mode I [9].

For this reason, mode II failure was investigated in this research on unidirectional carbon/epoxy based beams with a manufactured initial crack length. However, carbon/epoxy based structures are quasi-brittle in nature, indicating that failure is caused by fracture,

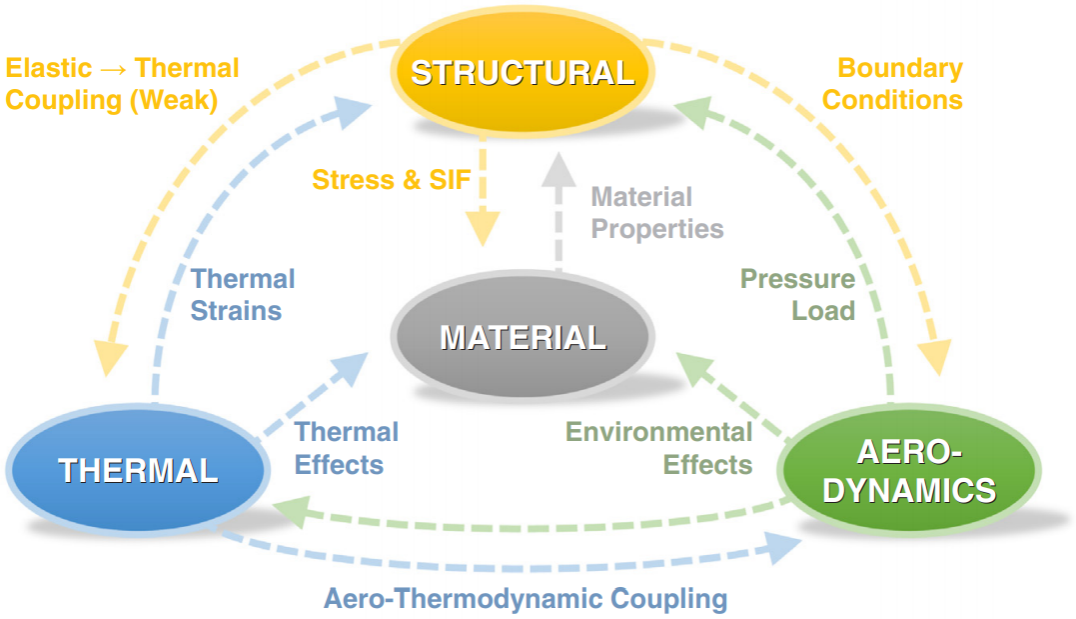

Figure 1.2: Schematic of relevant physics showing the coupling of aerodynamic, thermal, and structural effects [8]

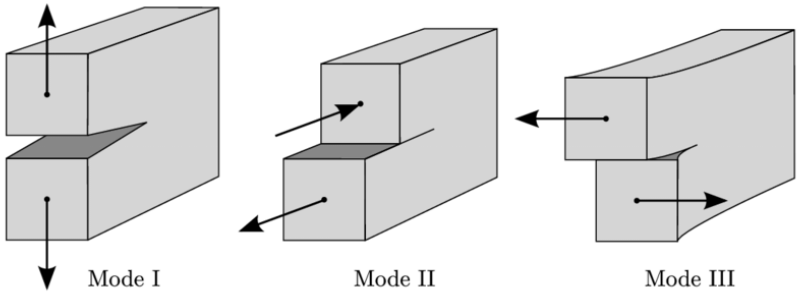

Figure 1.3: Modes of fracture

whose fracture front is surrounded by a large, non-linear Fracture Process Zone (FPZ) [10–12]. Because of this, these structures do not follow traditional Linear Elastic Fracture Mechanics (LEFM) theory, and instead fracture loads are greatly influenced by structure dimension [10–12].

1.3.1 Quasi-Brittle Fracture and Size Effect

LEFM is valid for brittle materials demonstrating linear elastic behavior [13]. Issues begin to arise for those materials exhibiting quasi-brittle behavior, initially discovered in concrete and later verified for a large number of materials at a laboratory scale including fiber and textile composites, nanocomposites, discontinuous fiber composites, bone, rocks, and many others [12, 14–27]. On a small scale, these materials demonstrate quasi-behavior, while on a large scale behave in a brittle fashion. This bridging of both small and large scale effects signifies the presence of a non-negligible characteristic length of the material, which characterizes the size of the non-negligible FPZ [14]. The effect of sizing is crucial to understand and incorporate, as the same material that may exhibit behavior corresponding to LEFM may result in small specimens of the same material demonstrating quasi-brittle or even quasi-ductile behavior [14]. LEFM fails to incorporate the influence of the FPZ that exists in smaller structures, and does not account for the pseudo-plasticity effects as size decreases. Figure 1.4 graphically shows LEFM theory on a log-log scale of strength with respect to structure size, depicting a negative linear relationship. However, at smaller sizes, geometrically scaled structures with a characteristic length, D, of the same material exhibit quasi-brittle and quasi-ductile behavior, which must be accounted for by Bažant's Size Effect Law (SEL) given in equation (1.1) [28].

$$\sigma_N = B f_t'(1 + D/D_0)^{-1/2} \tag{1.1}$$

Where this equation represents the function that bridges the two power laws between plasticity effects and LEFM theory. In this case, B is a dimensionless parameter and D is a geometric size of the structure and D_0 is a reference geometric size [14]. In terms of fracture characteristics, equation (1.1) becomes equation (1.2).

$$\sigma_N = \sqrt{\frac{E * G_f}{g'(\alpha_0)c_f + g(\alpha_0)D}} \tag{1.2}$$

Where E is the material modulus of elasticity, G_f is the material fracture energy, c_f is the effective FPZ size, D is the characteristic length of the structure, α is the crack length

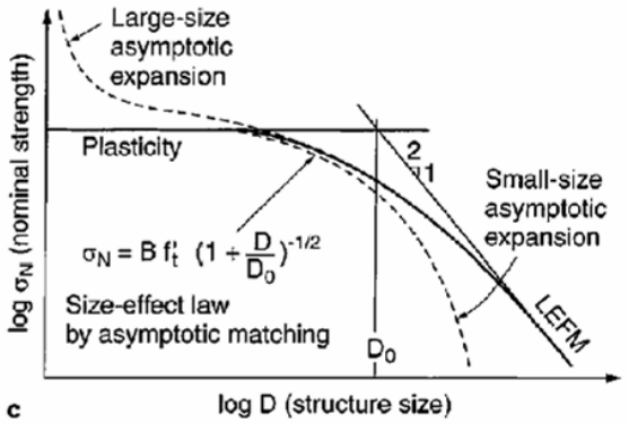

Figure 1.4: LEFM theory and Bažant's SEL, incorporating plasticity in smaller sizes [14]

normalized with respect to the characteristic length, g(α) is the dimensionless energy release rate, and g' is its derivative.

1.3.2 Cohesive Zone Model

In addition to structural dimension, requiring the imposition of the SEL, the stresses at the crack tip must be conceptualized. LEFM models an infinite stress at the crack tip, assuming a perfectly sharp crack [29]. This stress singularity presence contradicts what is understood for failure of materials, so instead techniques have been found to remove this issued stress singularity [29]. Utilizing a Cohesive Zone Model (CZM), the fracture process can be described without the presence of a stress singularity. Work pioneered by Barenblatt revolutionized fracture mechanics introducing the cohesive crack model using a vanishing thickness in front of the crack tip, where material failure is described by the separation of the two surfaces bordering the crack location and connecting at the crack tip [29, 30]. A traction-separation law governs the separation of the two cohesive surfaces by describing the traction and relative displacements of the surface, serving as a material property. A cohesive traction force contains the crack tip, causing the crack to propagate only when the separation at the crack tip reaches a critical value. A general relationship between the cohesive traction and surface displacement can be seen in Figures 1.5a and 1.5b.

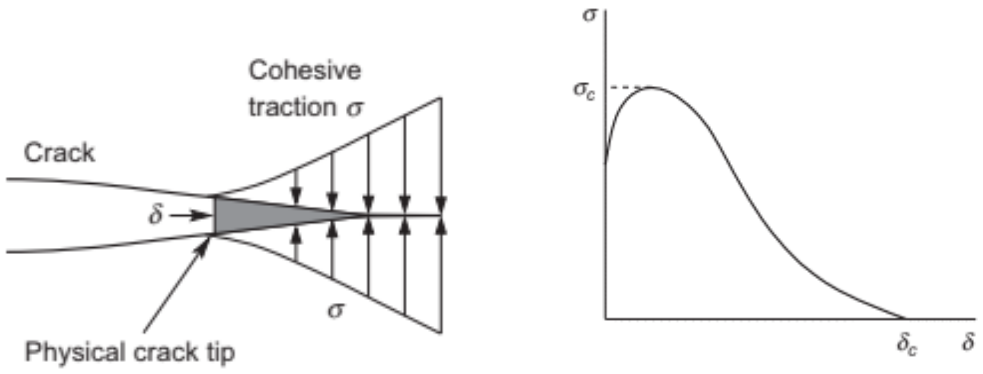

(a) Cohesive traction force

(b) Relationship between traction force and surface displacement

Figure 1.5: Traction separation law

The relationship seen is often derived phenomenologically, from experimental results and presupposed theory. CZM derivation often uses a linear softening model to describe the traction-separation behavior of quasi-brittle materials [29]. Although a linear softening model is typically used, this model can be adjusted to accommodate for plasticity or other experimental behavior by modifying the model to depict bi-linear or tri-linear curves depending on which best matches experimental results, exemplified in Figure 1.6. It has been shown that fracturing behavior in size affected structures is not just influenced by fracture energy, but also this cohesive law determination [21, 31]. A study by Deleo et. al found that the CZM of composites may require a bi-linear law due to the FPZ interference [31].

1.3.3 Fatigue

Aerodynamic loading in high-stress scenarios such as those encountered in hypersonic flight regimes often impose a cyclical, fatiguing stresses onto parts of the aircraft [8]. It is important to understand crack growth in a quasi-static manner to identify the effects of sizing, but the dynamics that surround fatigue cycles lending toward crack propagation must be understood for currently employed structures and materials. Paris et al. derived a relationship based

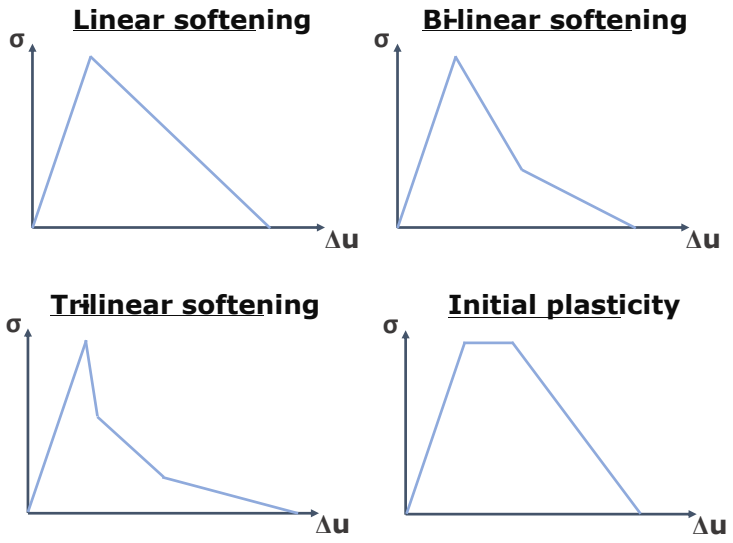

Figure 1.6: Different CZM types used in modeling techniques

on the stress-intensity factor ΔK and the rate of crack propagation da/dN, to identify the threshold values for stable crack growth [32–34]. An example of this relationship can be seen graphically in Figure 1.7.

The threshold values encapsulate Regime B, whose behavior is governed by the Paris Law power law. Regime A indicates stress intensity factors that lead to an infinite life of the material, while Regime C contains stress intensity factors that produce unstable crack growth [36]. This derived power law defines a region of the material after infinite life, where the crack growth and the crack growth rate can be predicted. This power law is rooted in energy considerations, which assumes a stress singularity at the crack tip, suggesting a critical stress singularity intensity factor at the crack tip to cause crack propagation [32]. Because of this initial assumption, this curve is accurate for linear elastic materials, like those modeled successfully with LEFM. For quasi-brittle and size affected materials, this curve may change due to the existing non-negligible FPZ that influences quasi-static test results [36, 37].

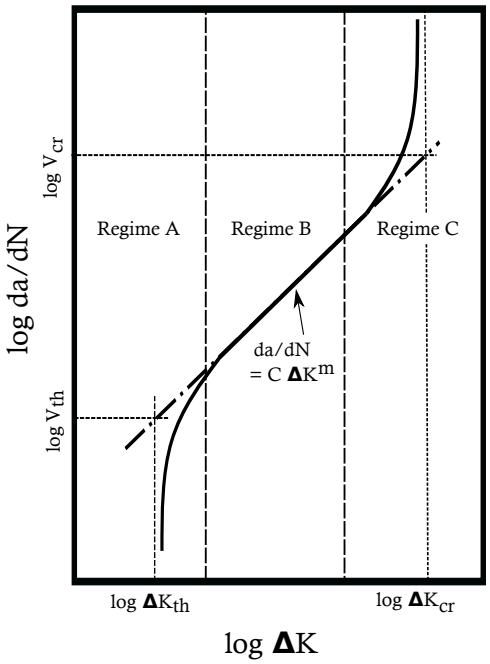

Figure 1.7: Generalized Paris Law curve for fatigue crack growth [32, 33, 35]

1.4 Current Completed Research

Extensive research has been conducted to characterize strain energies with mode I fracture utilizing the Double Cantilever Beam Test (DCB) [38–40]. Only recently a standardized test method for mode II fracture has been adopted to identify interlaminar strain energies [41]. End-Notched Flexure (ENF) tests, utilizing a 3-point bending fixture is outlined in ASTM D7905 [42], establishes a standardized test method to isolate mode II fracture under shearing forces. This reference provides a standardized test method to prevent mode mixity that can happen with incorrect crack dimensions [43]. Initial research has been conducted identifying appropriate crack inserts, specimen geometry, and size effect influences on these tests separately, which will be merged together in this research.

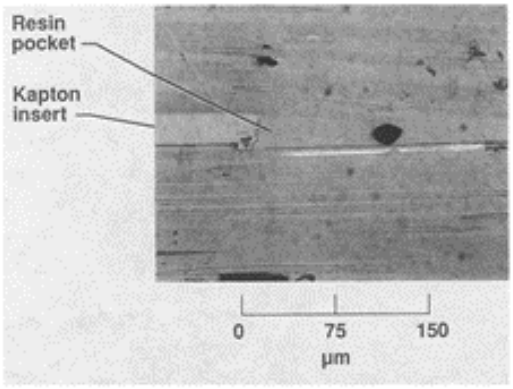

Figure 1.8: Resin pocket presence with 25 μm Kapton insert [44]

1.4.1 Teflon Thickness Affects

Murri et al. conducted initial ENF tests to isolate mode II fracture using Unidirectional (UD) 24-ply specimens of S2/SP250 glass epoxy composite with different size Kapton crack tip inserts [44]. The thicknesses of these inserts measured 13, 25, 75, and 130 μm respectively. Microscope images were collected at these different insert thicknesses and it was found that a "resin pocket" was observable for the Kapton inserts larger than 13 μm, seen in Figure 1.8.

Additionally, these ENF fracture tests did not indicate a limiting value for crack thickness, with thinner inserts resulting in lower fracture energy values [44]. This study found and recommended crack inserts to be no thicker than 13 μm, establishing a conservative approach due to an inconclusive limiting value for thickness [44]. This research provides insights regarding crack tip insert thickness but only tested specimens of the same geometry, with no size effect consideration.

1.4.2 ENF Testing Methods

Shivakumar et al. conducted research of different mode II fracture test and G_{IIC} calculation methods for UD composite laminates employing ENF, modified Japanese Industrial Standard (JIS), and ASTM D7905 to identify variances in these tests. These test methods all use an ENF specimen undergoing a 3-point bending load scenario but can calculate G_{IIC}

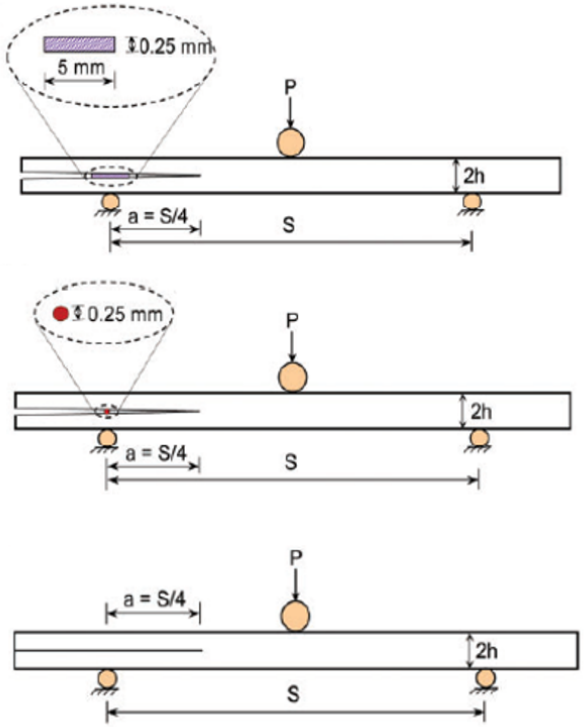

Figure 1.9: ENF specimen types used in Sivakumar et al. study [45]

in different ways, using both non-precracked (NPC) and precracked (PC) specimens. The differences in manufacturing of each specimen is highlighted in Figure 1.9.

Although each type has similar specimen geometry, the method to create the imposed crack tip is different. With the ENF method, a thick Teflon insert of defined dimensions is placed in the midplane of the specimen to create the manufactured crack. For modified JIS, a PTFE coated steel rod of diameter 0.25 mm is inserted, instead of a PTFE strip. From ASTM, a thin, Teflon insert is placed to create the entire crack geometry [45]. Using 20-ply UD layups from Hexcel AS4/8553 prepreg, fracture tests of each manufacturing method were conducted. It was found that fracture tests using the modified JIS rod-insert method introduced the mode I stress state, causing the G_{IIC} fracture toughness values to be lower than the ASTM values. Additionally, it was found that insert thickness and precracking affected the fracture toughness values, as well, identifying a 26% decrease in G_{IIC} for the PC versus

the NPC specimens [45]. These findings support those of Murri et. al, emphasizing the importance of crack insert thickness. However, no size effect investigation was performed on these specimens. It is important to note the influence of the NPC versus PC test specimens, as different behavior is observed by each. An example of these can be seen in Figure 1.10, which articulates the difference. The NPC specimens are the pristine, manufactured specimens whose crack tip is created through the use of a Teflon insert, seen in previous studies. PC specimens are made after the fracture test of an NPC specimen, which undergoes crack growth, as recommended by ASTM D7905 [42]. In order to identify the new, sharp crack tip, the Compliance Calibration (CC) method for crack length calculations must be performed. However, issues arise with conducting tests of PC specimens, as now micro-damage can exist in the homogeneous beam region due to the previous fracture test. This causes the CZM, which dictates fracture energy and crack growth, to change and produce test results that are inconsistent with the pristine NPC specimen. Additionally, the CC method, as shown later, produces multiple values for fracture energy for size affected specimens. This contradicts theory that claims G_{IIC} is a material property, and hence should exist as one value for each material, independent of geometry. For these reasons, only NPC tests will be conducted in this research.

1.4.3 Mode II Size Effect

Salviato et al. conducted size effect testing on ENF specimens to characterize mode II fracture behavior. These specimen dimensions can be seen below in Table 1.1, using a 2:3:5 scaling method [40]. These tests were conducted on DGEBA-based epoxy resin with a 2x2 twill layup, whose fracture loads can also be seen in Table 1.1.

Nonlinear behavior was observed prior to the fracture load, which was more pronounced for the smaller specimen sizes. This contributes to the presence of a non-negligible FPZ for smaller structure sizes [40]. Due to the FPZ interference, it was found that LEFM is no longer valid for smaller specimen sizes. This requires implementation of the SEL to account for the nonlinear FPZ that influences the fracture behavior [40]. Salviato et al. applied Bažant's Type II SEL to the collected ENF fracture data resulting in the following size

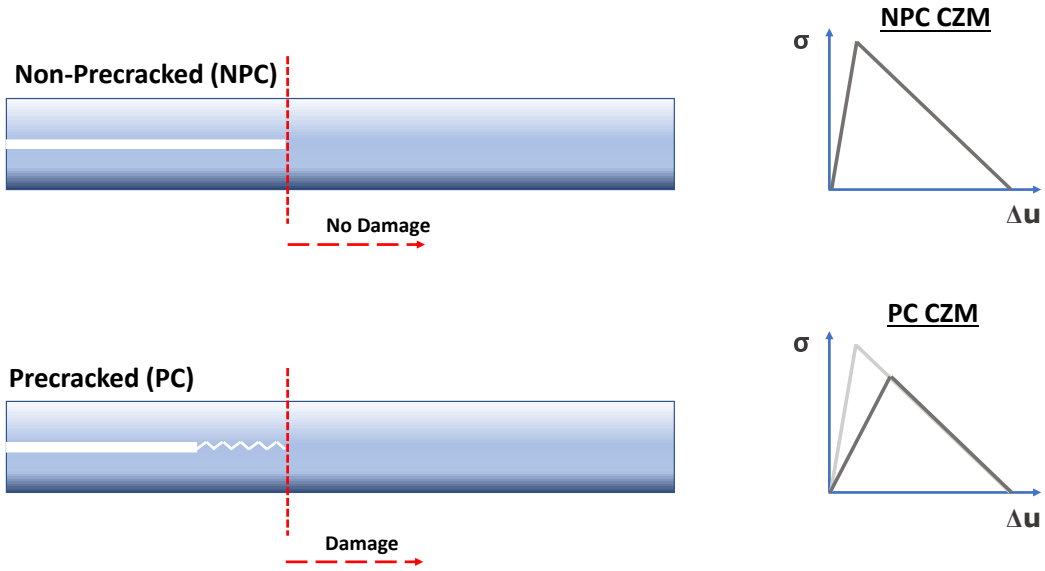

Figure 1.10: NPC and PC specimens with CZM changes

Size	Thickness (mm)	Gauge Length (mm)	Crack Length (mm)	Width (mm)	Avg Max Load (N)	Avg Nominal Strength (MPa)
Small	3.8	200	50	25	413	4.35
Medium	5.7	300	75	25	508	3.56
Large	9.5	500	125	25	776	3.28

Table 1.1: Geometrical specifications and results of ENF specimens by Salviato et al. [40]

effect plot seen below in Figure 1.11.

Additionally, it was found that the mode II fracture energy was 2.25 N/mm and an equivalent FPZ length of 33.51 mm for this material [40]. It is worth noting that the size effect specimens tested only approach the transition point between the pseudo-plastic limit and LEFM asymptote. These results are in excellent agreement with the SEL, but provides an opportunity for smaller dimensioned specimens to be tested past this transition point.

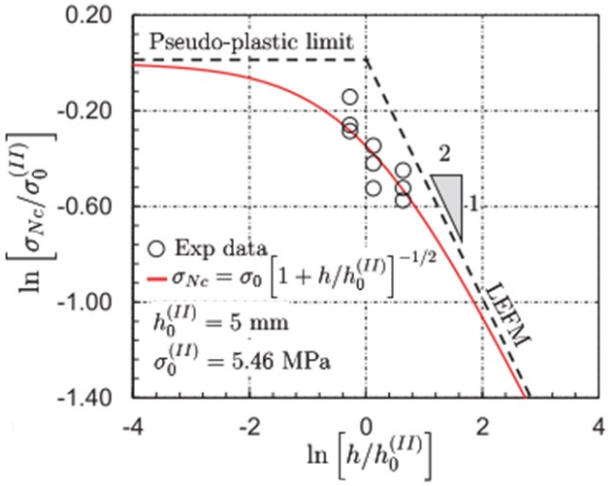

Figure 1.11: Size effect plot from ENF test results of Salviato et al. [40]

In addition to conducting experimental tests, Salviato et al. augmented these results with Finite Element Analysis (FEA) utilizing a CZM. A linear traction-separation law was used for mode II loading. This research found good agreement among peak loading between FEA simulation and experimental data, but acknowledged better correlation can be obtained using a bilinear cohesive law based on the recent findings of Qiao and Salviato [46]. The results using a linear traction-separation law were unable to capture the snap-back that occurs at the moment of crack propagation. It was recommended that a steeper decrease in shear stresses within the law would capture this result [40]. These results are important as they validate the SEL and identify some of the errors that are associated with LEFM in a small scale, necessitating the understanding and investigation of size effect for quasi-brittle materials.

1.4.4 Paris Law Size Effect

Guo et al. investigated the effect of scaling under fatigue conditions by identifying how scaling affects the Paris-Erdogan law [37]. Although not using ENF specimens, Guo et al. used Single Edge Notch Bending (SENB) specimens made of a thermoset polymer material [37]. Crack growth was monitored within the clear epoxy using a digital microscope, allowing

a direct measurement of the crack [37]. This crack growth and crack length information was used to construct the linear region of the Paris-Erdogan curves which can be seen in Figure 1.12.

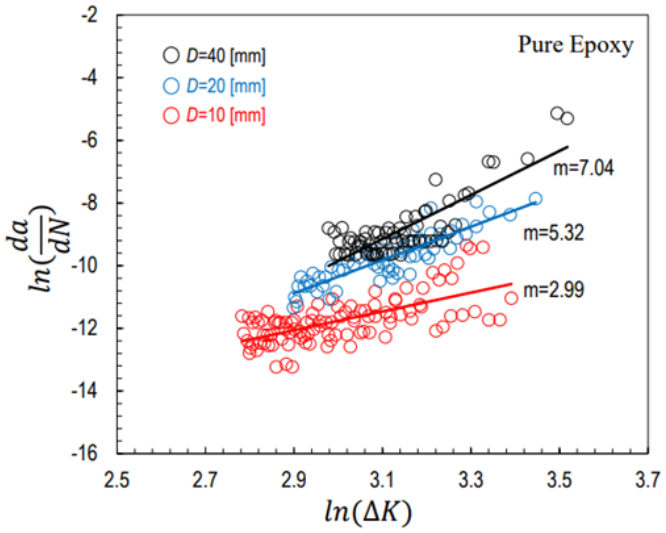

Figure 1.12: Paris-Erdogan linear results from Guo et. al [37]

Due to the nature of SENB tests, the stress intensity factor, K, was calculated for mode I, but it is worth noting the influence of size effect on these curves cause a shifting for each size specimen indicating the need to account for a non-negligible FPZ that exists at the crack tip [37]. The Paris law is typically expressed as a material property and hence a size adjusted Paris law was developed by Bažant and Kirane, which was used in this research [37,47]. The research of Guo et al. found an appreciable difference in Paris curves due to size effect, that mainly influenced C, in equation 1.3 but was unable to merge the three curves together using the adjusted Paris-Erdogan law. The adjusted law only adjusts C in the equation above, not the exponent n.

$$\frac{\mathrm{d}a}{\mathrm{d}N} = C\Delta K^{n}{}_{D} \tag{1.3}$$

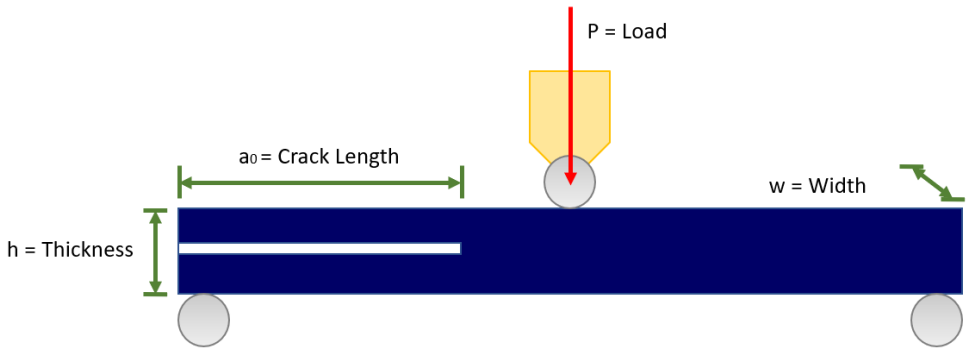

Figure 1.13: Quasi-Static Fracture Loading

1.5 Goal of Thesis, Remaining Chapters, and Motivation

Extensive research has been conducted on the more common, mode I fracture and failure for quasi-brittle materials, much less has been conducted for mode II. Only recently has a standard test method for ENF specimens been developed to investigate the fracture energy of mode II fracture, as well. Due to the nature of stress amplitudes experienced during in-flight loading and dynamic snap-through, it is imperative that these mode II material properties and crack propagation methods be robustly investigated. This paper aims to test many different variables surrounding fracture energy identification and crack propagation to validate previous results and make new conclusions, all under the same research. To test this, there exists three test cases: quasi-static fracture, quasi-static fatigue, and forced-dynamic fatigue, depicted in Figures 1.13 and 1.14.

First, different crack sizes will be tested by use of different thicknesses of the Teflon insert to identify the effects of crack thickness on interlaminar fracture energy under quasi-static fracture conditions. Second, ENF size effect testing will be conducted on small-scale and large-scale specimens to observe the correlation of the SEL in smaller sizes under the Pseudo-plastic limit, also under quasi-static fracture. This testing will also utilize DIC technology to progress CZM development for T700 and T800 carbon/epoxy prepreg materials. Third, an

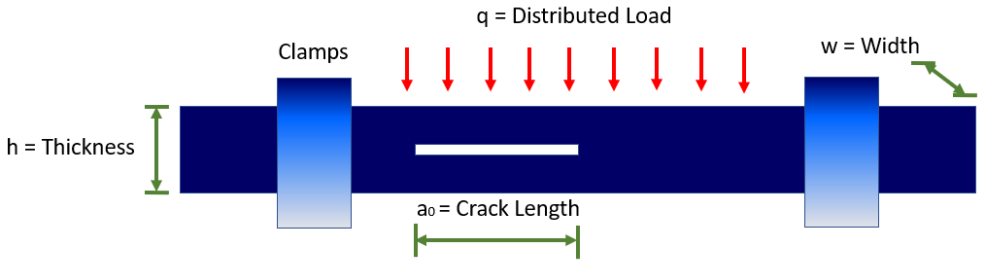

Figure 1.14: Quasi-Static Fatigue Loading

initial fatigue study will be conducted to construct a Paris-Erdogan curve of crack growth for T800 carbon/epoxy material using quasi-static fatigue methods. Forced-dynamic fatigue specimens are manufactured, but must be tested at the Air Force Research Lab at a later date.

This paper is organized to identify a traceable line of research investigation beginning with the in-house manufacturing process in Chapter 2 to create the test specimens used during the quasi-static fracture, fatigue, and forced-dynamic fatigue cases. This chapter will articulate the design parameters that drove specimen dimension, as well as demonstrating the hands-on work required to manufacture testable carbon beams. Chapter 3 will explain the quasi-brittle fracture testing and analysis of the manufactured beams for Teflon effects and size affected specimens. Comparisons of the fracture energies will be made, and Teflon thicknesses will be compared under Bažant's Size Effect Law. Chapter 4 introduces the preliminary quasi-static fatigue testing and analysis. This serves to find the effect of specimen sizing on the Paris Law curves which govern fatigue crack growth. Key points of this research will be summarized in Chapter 5.

Chapter 2

MANUFACTURING

2.1 Introduction and Overview

This project focuses on the experimentation of carbon composite ENF beams, which were manufactured in-house at the University of Washington (UW) in the Mechanical Engineering (ME) composite shop. The manufacturing process follows that of typical prepreg carbon plate layup, guided in ASTM D5687 [48]. Utilizing various carbon prepreg material, each ply is set atop each other to achieve a desired thickness. Each plate is then baked in the autoclave to ensure proper curing, allowing usable specimens to be cut from the manufactured plate. The dimensions of each specimen depend greatly on the test and data being taken, which will be discussed later in this chapter. For this research, three different sets of specimens were manufactured to help facilitate different test goals. These included quasi-static tests, forced-dynamic fatigue tests, and contact fatigue tests. This chapter outlines the three specimen types: quasi-static fracture with two different Teflon sizes, forced-dynamic fatigue test specimens, and the quasi-static fatigue test specimens. The dimensions and design considerations for each specimen type are also discussed. Then, an explanation of the in-house manufacturing process will be explained that was conducted to create each type of test specimen.

2.2 Specimen Types

The experimental nature of this project required many different specimen types and dimensions. An experimental approach was taken to characterize the effect of a sharp vs. notched crack tip, requiring plates to be manufactured with different Teflon thicknesses. The ASTM Standard D7905 mode II fracture of ENF specimens presents a maximum allowable Teflon thickness of 0.0005 in (12.7 μm), which was followed in the manufacturing process [42]. An image of the ENF beam model can be seen in Figure 2.1 under quasi-static load conditions.

An additional investigation was conducted to identify the fatigue limits on carbon/epoxy beams in both forced-dynamic, and contact fatigue testing.

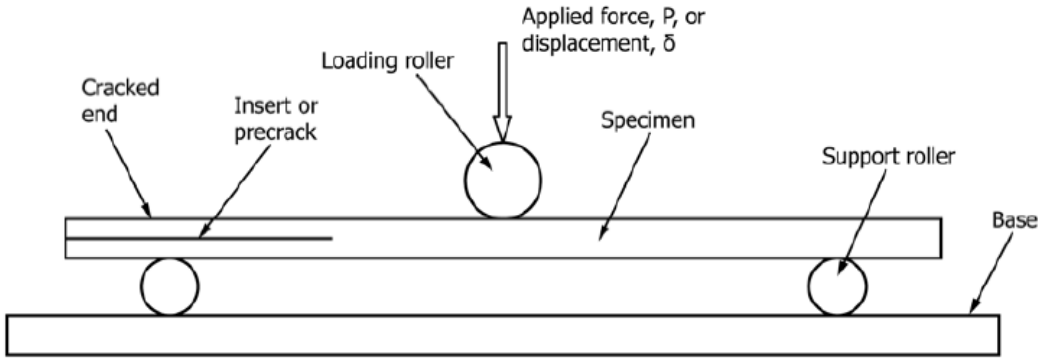

Figure 2.1: ENF Beam Model

2.2.1 Quasi-Static Specimens

The initial investigation served as a continuation of previous work conducted at UW to identify the size effect of composite materials. Previous research indicates that the strength of ENF specimens, like those tested here, are not scaled according to LEFM. It is found that an enhanced pseudo-ductility is present in smaller sized specimens, while larger specimens behave in a more brittle fashion [12]. This size effect behavior is due to the size of the

Size	Target Width (mm)	Actual Width (mm)	Target Thickness (mm)	Actual Thickness (mm)	Number of Plies
1	25	23.14	1.2	1.05	8
2	25	23.89	2.4	2.18	16
3	25	25.39	4.8	4.61	32
4	25	24.96	9.6	9.45	64

Table 2.1: T700G Quasi-Static Specimen Dimensions

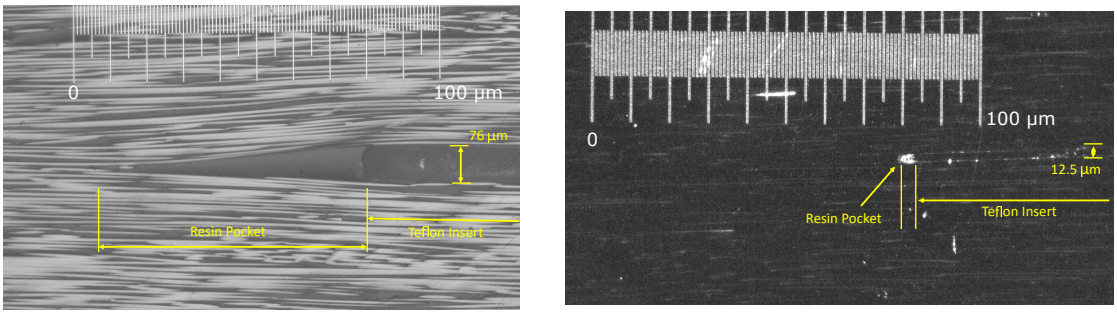

(a) Thick teflon insert displaying resin pocket

(b) Thin teflon insert showing no resin pocket

Figure 2.2: Teflon inserts affecting resin pocket presence

FPZ that exists at the crack tip, which becomes significant in smaller structures, causing an underestimation of fracture energy following LEFM theory [40]. These quasi-static tests served as smaller size specimens, augmenting the work of a previous student, helping identify the effects of the FPZ surrounding the crack tip, as well as developing a reliable CZM to predict future fracture loads and moduli. Using Toray T700G-12K material with 150 gsm and 35% resin content, the specimen geometry was outlined in ASTM D7905. Utilizing this test standard, a scaling law was formulated to re-dimension the specimens with smaller gauge length, crack length, and thickness. A table of the four sizes can be seen in Table 2.1.

Additionally, two different Teflon sizes were used to investigate the effect of thickness on fracture energy. The ASTM test standard requires a Teflon insert for the induced crack to be $<$0.0005 in (12.7 μm), and two Teflon inserts were chosen to surround this measurement. Thicker Teflon sizes showed the presence of a resin pocket surrounding the Teflon tip, seen in Figure 2.2a.

This corresponds to the data received by Murri and Martin [44], depicting resin pocket presence with thicker Teflon inserts. With thinner Teflon inserts ($<$13 μm), the resin pocket cannot be observed even under highest magnification in Figure 2.2b. The presence of the resin pocket affects crack propagation and fracture energy, a fracture line can be observed on the thicker Teflon specimen, resulting in a crack growth on the radius of the notch at the highest stress concentration, seen in Figures 2.3a and 2.3b, indicating the importance of

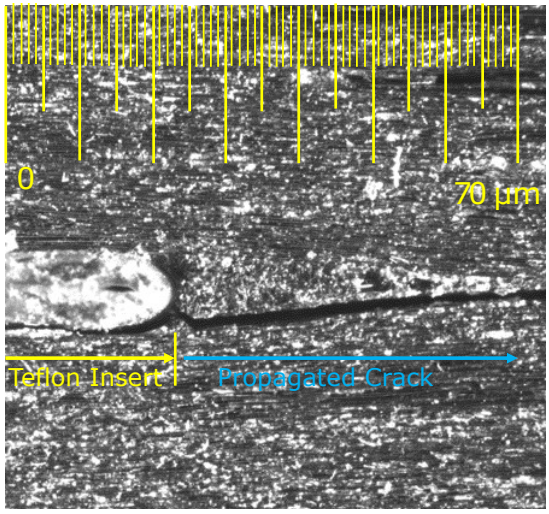

(a) Crack propagation along teflon radius

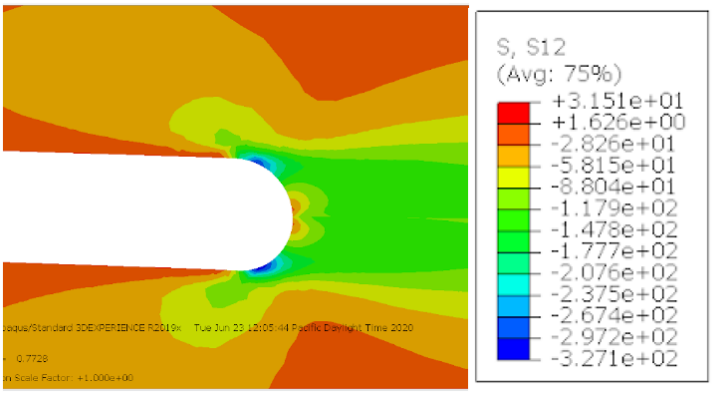

(b) ABAQUS simulation of ENF beam teflon radius, showing high stress concentration

Figure 2.3: Correlation of experimental and simulated results for crack growth location

the Teflon insert sizing. It is expected that a thinner Teflon insert will have a lower fracture energy, as the thinner Teflon results in crack growth at the tip, satisfying the thickness requirement of the ASTM Standard.

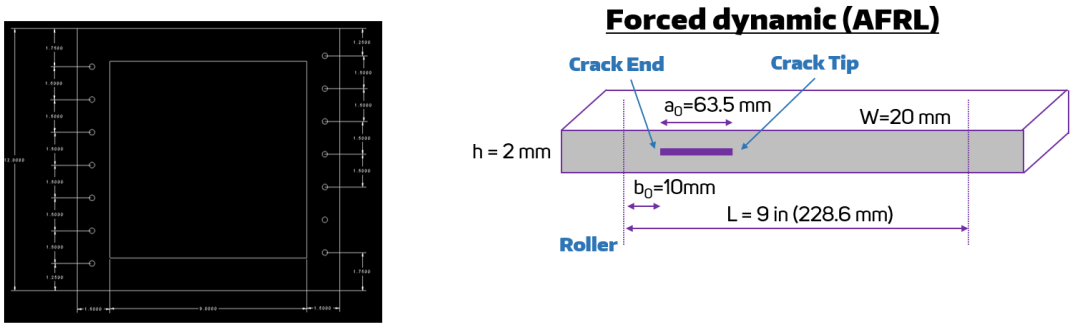

(a) Fixture geometry of AFRL shaker table

(b) Dimensions of forced-dynamic fatigue specimens

Figure 2.4: AFRL specimen design

2.2.2 AFRL Specimens (Forced-Dynamic Fatigue)

More specimens were manufactured using Toray T800S-24K material with 160 gsm and 35% resin content to be used for forced-dynamic fatigue tests at the Air Force Research Laboratory (AFRL) at Wright-Patterson AFB, OH. These specimens were manufactured using a different geometry due to the test equipment parameters and nature of the test type, but used the same thin Teflon as successfully employed in the previous quasi-static specimens. Details of the fixture can be seen in Figures 2.4a and 2.4b.

These specimens would be loaded inertially on a shaker table, inducing a load through dynamic oscillations, rather than a contact roller. Because of this, a specimen was needed to be both heavy enough such that the G loading would have a non-negligible effect on the specimen, while not being too strong that the G loading induced stress could cause crack propagation. Preliminary calculations were made to identify the maximum shear value during the fracture load for the different size specimens, found in Table 2.2.

$$\tau_{max} = \frac{VQ}{It} \tag{2.1}$$

These calculations served as a reference to shear values needed to grow the crack in a

Size	Crack Length (mm)	Span (mm)	Width (mm)	Thickness (mm)	Max Load P_{cr} (N)	τ_{max} at P_{cr} (MPa)
2	20	72	24.13	2.18	615.65	8.77
3	40	144	25.35	4.63	1159.51	7.41
4	80	288	24.91	9.43	1907.84	6.09

Table 2.2: Maximum shear values at beam locations under forced-dynamic loading

forced-dynamic fatigue setting. From previous shaker table data, the distributed load, G loading values, and associated buckled rise values were known, from which theoretical shear values were calculated seen in Table 2.3. For fatigue, a lower threshold is needed for shear to propagate the crack and it was found that a larger buckled rise would contribute to the largest shear value at the roller, ranging between 20-30% of the quasi-static maximum shear. Testing at the AFRL aimed to confirm that these dynamic loading values would propagate the crack under fatigue conditions found in Table 2.3, where the crack locations can be seen in Figure 2.4b.

Rise (mm)	q (MPa)	q (G)	τ_{max} at Roller (MPa)	τ_{max} at Crack End (MPa)	τ_{max} at Crack Tip (MPa)
1	0.000882	28	0.076 (0.86 - 1.2%)	0.069 (0.79 - 1.1%)	0.034 (0.39 - 0.56%)
1.5	0.00288	92	0.247 (2.8 - 4.1%)	0.225 (2.6 - 3.7%)	0.110 (1.3 - 1.8%)
2	0.00678	216	0.581 (6.6 - 9.5%)	0.530 (6 - 8.7%)	0.258 (2.9 - 4.2%)
2.5	0.0127	405	1.089 (12.4 - 17.9%)	0.993 (11.3 - 16.3%)	0.484 (5.5 - 7.9%)
3	0.02035	650	1.745 (19.9 - 28.7%)	1.592 (18.2 - 26.1%)	0.775 (8.8 - 12.7%)

Table 2.3: Maximum shear values at beam locations under forced-dynamic loading

2.2.3 Fatigue Specimens (In-House)

Additional carbon specimens were manufactured to investigate fatigue life under contact loading, to be tested in-house at the UW. These specimens were manufactured using Toray T800S-24K material with 160 gsm and 35% resin content, and followed the size effect scaling used for the quasi-static fatigue specimens. These specimens utilized the same thin Teflon insert as used in the previous two cases. In the case of the quasi-static specimens, the thickness was consistently under the target value for size effect. With each ply measuring 0.15mm, two additional plies, one on each side of the midplane, were incorporated to better achieve the size effect target thickness. The ply numbers used and their respective dimensions can be seen in Table 2.4.

Size	Target Width (mm)	Actual Width (mm)	Target Thickness (mm)	Actual Thickness (mm)	Number of Plies
1	25	25.68	1.2	1.48	10
2	25	24.63	2.4	2.78	18
3	25	25.23	4.8	5.42	34

Table 2.4: T800S Fatigue Specimen Dimensions

The thickness values were greater than the target thickness after the addition of two plies likely due to the higher fiber weight contributing to a slightly thicker ply. Despite the difference, this material will still be characterized using quasi-static testing prior to fatigue to establish baseline fracture loads and compliance tests results to be used later in calculation.

2.3 Manufacturing Process

The manufacturing of carbon plates follows the same procedure for the in-house closed molding technique at UW, independent of geometry, which can be seen in Figure 2.7. Prepreg material used is stored in an industrial freezer to ensure longer shelf-life of the material and mitigate risk of precuring during storage. Because of this, the material rolls must be thawed prior to working. To do so, a fan is placed in close proximity to the prepreg roll in ambient

temperature for 1-2 hours. Once thawed, this prepreg material is cut using a CNC fabric cutter to precisely cut the roll into predetermined plate sizes, later to be dimensioned for carbon beams. After, these prepreg plies are laid up onto a metal plate, following the material sandwich method seen in Figure 2.5.

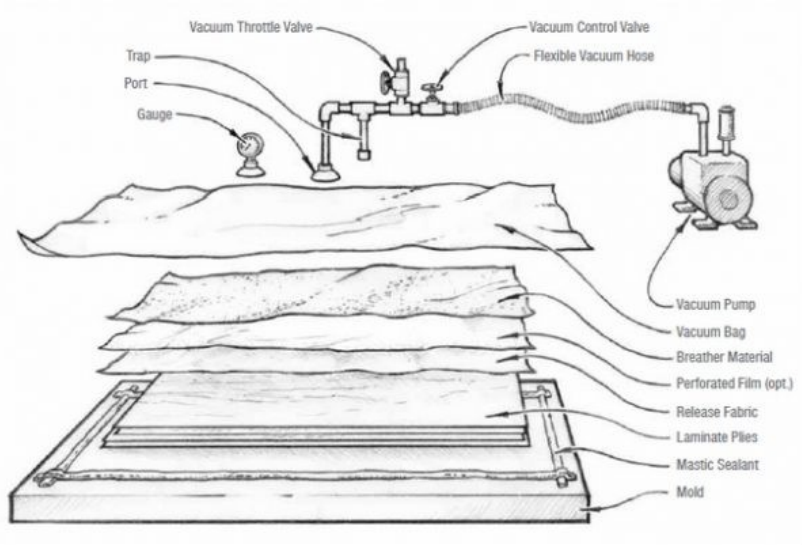

Figure 2.5: Vacuum bag layup technique for closed molding carbon plate manufacturing [49]

After each 8-10 plies, a debulking period removes any voids present in the layup over a 1+ hour period, providing pressure onto all sides of the layup under vacuum. Once at the midplane, a Teflon insert is placed in a predetermined location to achieve a desired precrack length in the final test specimens. Ply stacking continues until the desired thickness is reached, and an appropriate autoclave bake cycle was determined by the manufacturer's requirements. This involves applying temperature and pressure conditions to properly cure the plates and to create a usable, load-bearing material. An example of one of these cycles for T800 material can be seen below showing the ramping temperatures and pressures and holding for an extended period of time.

After the completed autoclave bake, the plates are removed from the autoclave and released from the working surface. Then, the plates are dimensioned and cut using the in-house tile saw to create each carbon beam with desired geometry. After cutting the

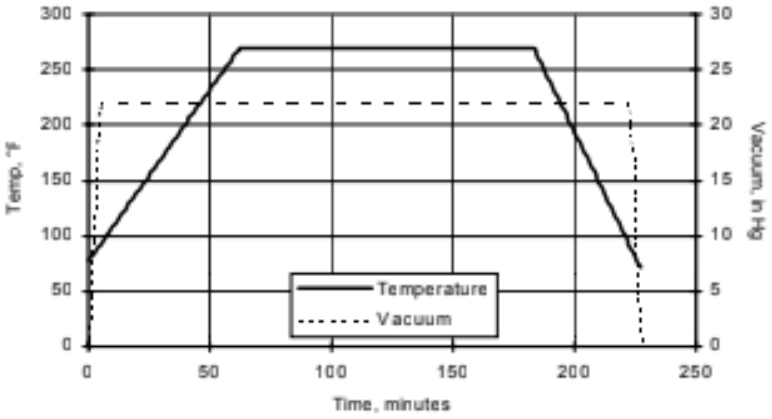

Figure 2.6: Example cure cycle for T800 material [50]

specimens to the desired geometry, each are cleaned and tabulated with measurements taken with calipers at small intervals along each beam. ASTM D7905 specifies measurements to be taken at six intervals measuring the thickness of the beam for both the top and bottom sides [42]. Additionally, width measurements are taken at these six points, as well. However, this is only recommended for the single-size specimen defined in the ASTM manual for mode II fracturing, which defines a gauge length of 100 mm. For size affected test specimens as discussed in this research, these measurements are scaled appropriately. These precise dimension measurements enable further calculations from the load-displacement data obtained in testing. An image of this manufacturing process can be seen in Figure 2.7.

Digital Image Correlation (DIC) software that is used during testing requires a speckle pattern to be displayed on the face of each beam allowing local displacement tracking to calculate full-field strain. Each specimen is masked off on all sides but one face of the beam, where a white background is painted using white spray paint to promote good contrast from the later painted black speckles. For larger specimens (Sizes 3 & 4), each specimen is carefully speckled using black spray paint for use with macro-scale 3D DIC equipment. To speckle properly, the spray can is positioned for use about 4 feet away from the white-painted edge of the specimen. For best results, the nozzle is directed slightly off center of the

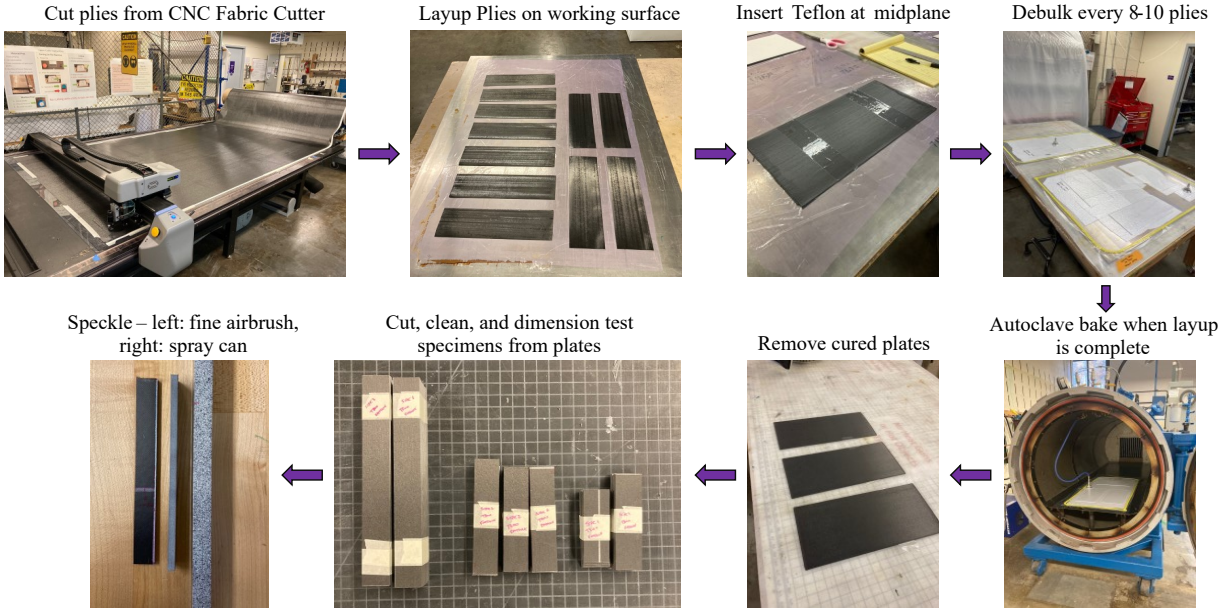

Figure 2.7: UW in-house manufacturing cycle for carbon composite plates

specimen to prevent larger, undesirable paint "blotches" to adhere to the face of the beam. The paint is sprayed in short bursts to promote fine speckles, and to control the amount of paint applied to the surface. Finished specimens should have 50-60% black speckles, making the beam appear a homogeneous grey from afar. It is important for an even distribution of fine speckles as this enables the DIC software to track the full-field strain data, necessary for accurate CZM development. For smaller specimens (Sizes 1 & 2), a micro-scale 2D DIC microscope tracks displacement, requiring an airbrush application to create finer speckles to be observed and tracked underneath the microscope. Successful speckling utilizing the airbrush is an iterative process and depends on the condition of the airbrush, air pressure, and ink used. In this research, best results were found after thoroughly cleaning the airbrush and using a 0.5 mm nozzle and needle paired with Creatix 5211 Opaque Black airbrush ink. Using 40 psi of air pressure, the airbrush button can control the air outlet and can be pulled

to adjust the amount of ink-flow. To promote a homogenous speckle pattern, the needle was adjusted such that a small amount of ink could pass through the nozzle without having to pull the airbrush lever to increase the ink-flow. This enabled a very fine spray of black ink which was then applied to the white face of the beam. Positioned only about 6" away from the beam face, multiple passes were made on the face of each specimen until a light grey hue was observed on the face. Specimen speckling is often regarded as "more technique than procedure", but is paramount to achieving high-quality data from the DIC methods to enable CZM formulation. Once properly speckled, images are taken during the loading scenario of each specimen tracking the relative displacements of the speckles on each beam to calculate the full-field strain values from each test. These are the images assisting to create an accurate CZM for the material. In summary, the following specimens were designed, manufactured, and prepared for testing:

- Quasi-static fracture specimens manufactured from T700G carbon/epoxy prepreg, using 76 μm thick Teflon for sizes 1,2,3, and 4.

- Quasi-static fracture specimens manufactured from T700G carbon/epoxy prepreg, using 12.5 μm thin Teflon for sizes 1,2, and 3.

- Forced-dynamic fatigue specimens manufactured from T800S carbon/epoxy prepreg, using 12.5 μm thin Teflon for sizes 1,2, and 3 of thicknesses 1.0, 1.5, and 2.0 mm respectively.

- Quasi-static fatigue specimens manufactured from T800S carbon/epoxy prepreg, using 12.5 μm thin Teflon for sizes 1, 2, and 3.

Chapter 3

MODE II QUASI-BRITTLE FRACTURE OF ENF SPECIMENS

3.1 Introduction

This chapter aims to describe the methodology used to conduct fracture tests and model validation for ENF specimens undergoing mode II failure in a 3-point bending load scenario. Using the manufactured specimens described in Chapter 2, NPC tests were conducted in accordance to ASTM D7905 [42]. Utilizing the CC method, one can calculate the Interlaminar Fracture Toughness, G_{IIC}, from the load-displacement data for the NPC specimens. This method provides different fracture toughness values for each size specimen, contradicting the theory that fracture toughness exists as a material property. Due to the inconsistency of the CC method and the damage created during fracture testing, only NPC test specimens were tested, discussed more in Chapter 1 and Figure 1.10. Instead, Bažant's Type II SEL must be used to account for the specimen sizing. This is exceedingly important for size effect specimens as the G_{IIC} value is influenced by the non-negligible FPZ in smaller sized specimens that surround the crack tip [**?**, 55]. Additionally, DIC data will be collected to create a full field strain view of each beam. This information will then be used to develop a robust failure model for crack growth simulated with a CZM, describing the damage propagation along the FPZ with a traction-separation law [51].

3.2 Experimental Setup

ENF fracture tests were conducted in-house using the manufactured carbon beams as shown previously. For smaller size specimens (sizes 1 & 2), fracture tests were conducted on the Psylotech μTS load frame utilizing 2D microscopic DIC with max resolution of 0.025 μm. For larger specimens (sizes 3 & 4), fracture tests were conducted on the Instron 5585H load frame, utilizing 3D DIC from VIC 3D with a max resolution of 10 μm. All specimens were subjected to a 3-point bending load, with gauge lengths defined in Table 2.1.

3.2.1 Micro DIC

Size 1 & 2 specimens were fracture tested on the μTS micro-load frame in conjunction with 2D DIC. The micro frame was chosen for the smaller specimens to better capture a refined image and loading data, whose size was too small for the 3D DIC cameras for proper data acquisition of the small beam faces and speckle pattern. Additionally, the microscope allows a unique area of interest, capturing the damage propagation in the local region near the crack tip, at the micro scale. In order to have the correct gauge length and CC crack length, a new fixture was designed and manufactured to accommodate the size effect test matrix. A 3D printer was opted for use instead of manufacturing fixtures out of aluminum for its rapid prototyping advantage and low cost association. Fixtures were designed in Fusion 360 and printed at 85% infill to accommodate the 36 mm and 72 mm gauge lengths for the size 1 and 2 specimens, respectively, while still maintaining necessary compliance. The 3D printed design also allowed for a wider specimen of 25 mm, supporting the specimen geometry declared by ASTM D7905 which was not previously achievable by the old fixture. An additional fixture for the loading roller was also designed and manufactured These fixtures can be seen in Figure 3.1.

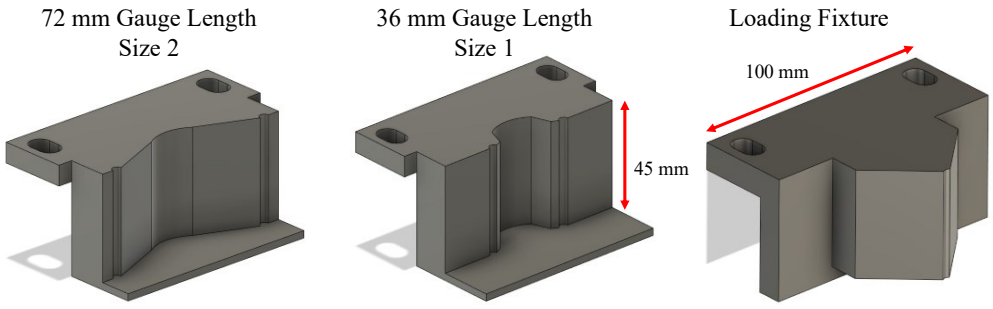

Figure 3.1: 3D printed loading and support fixtures

A compliance study was conducted on these fixtures to ensure adequate compliance with respect to the carbon beam specimens, as outlined in ASTM D7905, which requires the

fixture compliance to be less than 3% of the specimen compliance. Images of these fixtures can be seen in the DIC setup in Figure 3.2.

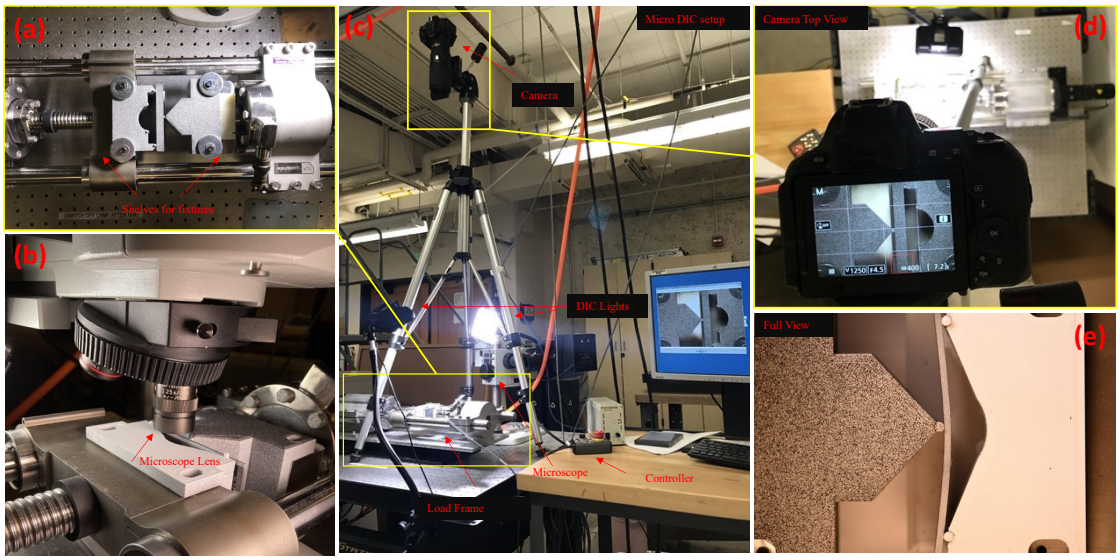

Figure 3.2: μTS micro-load frame setup with camera and microscope

Each fracture test was conducted by placing the receiving roller fixture and loading roller fixture onto the shelves of the actuating portion of the uTS frame. A screw was placed in one hole of the receiving fixture to prevent lateral movement of the fixture which was identified during an initial investigation. No other screws fixed the 3D printed pieces in place, to prevent compliance changes under loading. Instead, each specimen was preloaded between 30-40 N to ensure a proper interface without gaps between the 3D printed fixtures and the frame actuating shelves. Figure 3.2a shows the frame with all four screws in place during the compliance testing investigation, with Figure 3.2b displaying no screws to affix the loading and support fixtures. Compliance calibration tests were conducted without DIC for use in later calculation. Afterwards, lighting was adjusted to promote visible, high-quality speckle images taken during loading and used during post-processing. The narrow clearance between the microscope lens and specimen results in a very high sensitivity to

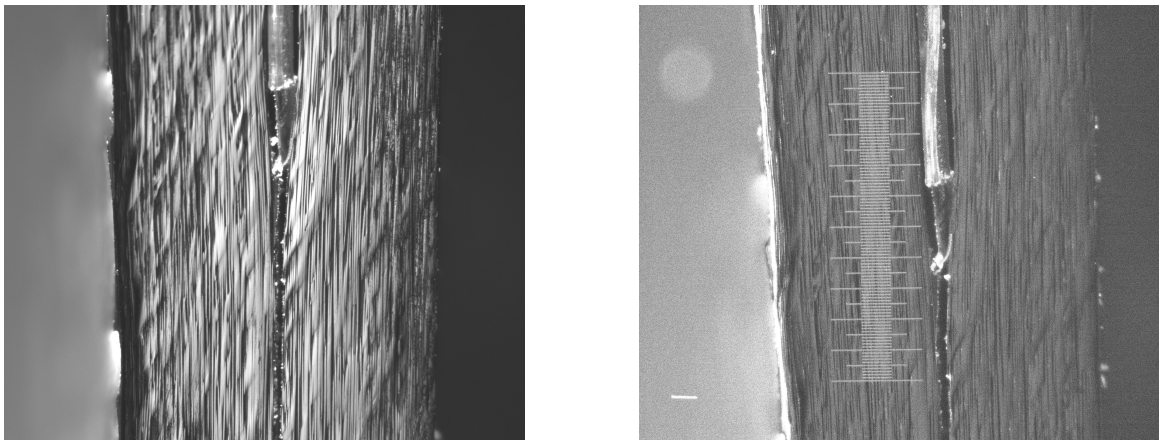

(a) Polished specimen with adjusted lighting for better reflection

(b) Cleaned and hand-sanded specimen with adjusted lighting concentration

Figure 3.3: Specimen preparation and lighting effects under microscope

light to accurately capture the crack tip. It is imperative that the lighting be properly adjusted so the crack tip will be observed and the DIC speckles will be distinct for accurate full-field strain calculation. This process utilizes two camera/video LED lights to properly illuminate the beam face under the microscope. These lights may be adjusted for brightness and different shades can be placed to adjust the hue as necessary to achieve optimal lighting. Differences in both lighting and polishing of prepared specimens can be seen in Figures 3.3a and 3.3b.

Both microscope images and full-field views were collected during various tests. The microscope was focused at the crack tip location to capture the specimen movement during the loading cycle and the size of the FPZ, later used during post-processing in the VIC 2D software for DIC images. Once good lighting and proper specimen loading was achieved, each fracture test was conducted with a 10 min ramp-loading cycle, which continued past the peak load to observe the post-peak behavior. This loading rate satisfied the ASTM defined requirement of 0.5 mm/min. This load-displacement data was later used to calculate the fracture energy and size effect curves, with the DIC images aiding CZM validation and FPZ size identification.

3.2.2 3D DIC

Size 3 & 4 specimens were fracture tested on the Instron 5585H load frame at the UW ME laboratory. The size of these larger specimens allowed the usage of 3D DIC cameras for speckle tracking, enabling a full-field strain view for each test specimen. This process involves orienting and calibrating two cameras to focus on the test specimen, while adjusting lighting such that the speckles on the face of the beam can be accurately tracked throughout the loading cycle. An image of this test setup can be seen in Figure 3.4. Following ASTM D7905, these tests had a 10 min loading, and 5 min unloading cycle, for each specimen, during which pictures from each camera are taken to be later used for post-processing. Similar to the micro DIC setup, each test specimen was subject to two compliance calibration tests, and one fracture test at different pre-determined crack lengths. Data acquisition continued past the crack propagation to observe the post peak behavior which would later be matched in modeling efforts.

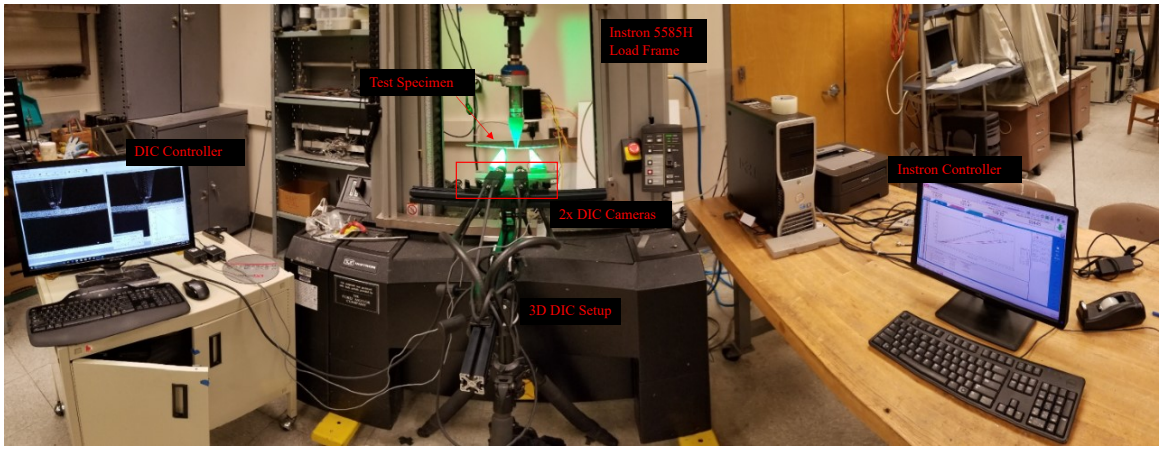

Figure 3.4: 3D DIC test setup for larger size ENF specimens

3.3 Test Results

Each fracture test yields load and displacement data for the associated specimen. Due to the nature of destructive tests, once the peak load is reached and unstable crack propagation occurs, the specimen cannot be tested again under the same conditions. Although we can predict crack growth lengths from theory, it is impossible to observe the actual sharp crack tip location without the use of a Scanning Electron Microscope (SEM) or similarly powerful equipment according to the ASTM manual for ENF testing. The load-displacement data obtained from each test allows the fracture energy to be calculated for each specimen using the CC method as recommended by the ASTM manual, but is highly dependent on specimen geometry which is observed in these test results [42]. To capture the effects of the non-negligible FPZ size primarily affecting smaller specimens, Bažant's Type II SEL must be used to accurately describe the mode II fracturing behavior that becomes inaccurate using classical LEFM methods [52]. This size effect method only requires the peak load for crack propagation, and hence eliminates the error in approximating the location of the crack tip, providing a more robust method. Additionally, the multiple fracture energy values obtained from LEFM and the CC method contradicts the theory that fracture energy is a material property and thus a single value for a specific material.

Prior to this research, fracture tests were conducted on the larger ENF specimens, sizes 3 and 4. To continue the size effect research, sizes 1 and 2 were tested on the μTS micro-load frame, using the same UD carbon layup and same thick Teflon inserts of 76 μm thickness. Seen in Figures 3.5a and 3.5b, the load displacement curves can be observed. Similar behavior is demonstrated in size 3 and 4 load-displacement curves, and is worth noting the instance of unstable crack propagation that occurs at the peak load. Depicted by a sudden drop in the positive-linear curve, snap-back instability occurs at the moment of crack propagation. Due to the fixture constraints, this is shown as a sudden vertical drop in the load path, rather than an equilibrium path and translation to kinetic energy from the system [52]. A table of the peak loading values for sizes 1-4 can be seen in Table 3.1. Variations in peak load occur mostly due to differences in geometry of each specimen. Because diligent dimensions are recorded for every specimen, these variations still help to provide accurate values for

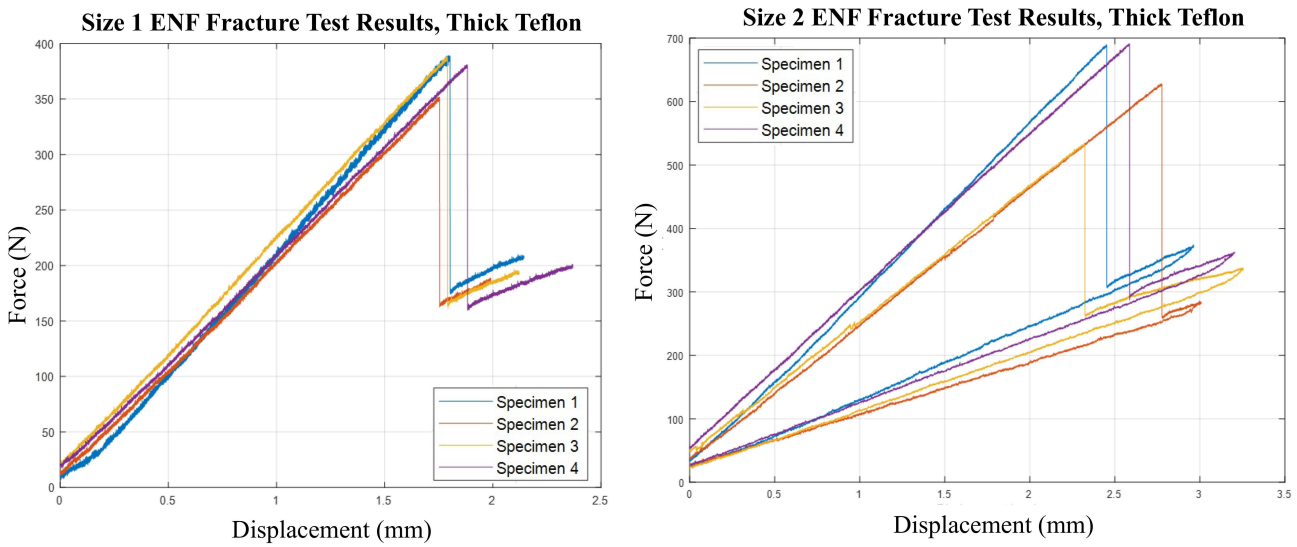

(a) Size 1 Load-Displacement test results

(b) Size 2 Load-Displacement test results

Figure 3.5: Fracture test results of thick Teflon T700 specimens

the interlaminar fracture energy, since these equations respond heavily to specimen length, width, and thickness.

Size	Number of Specimens	Avg Fracture Load (N)	Standard Deviation (N)
1	4	377.6	17.4
2	4	615.7	74.6
3	3	1159.5	8.34
4	4	1907.9	106.1

Table 3.1: Average fracture loads for sizes 1-4, thick Teflon

The same quasi-static tests were conducted on the T700 specimens with the thinner Teflon insert (12.5 μm), for which the data can be seen in Figure 3.6a - 3.6c. The same trends were observed, with a peak critical loading value causing crack propagation, with

only slight peak value variation. The average fracture loads of the thin Teflon specimens can be seen in Table 3.2, which show slight variation from the thick Teflon specimens in the previous table. In addition to Teflon size variation, these discrepancies are also due to specimen geometry, as this can have a significant influence to the critical loading values. In the next section, the specimen geometry will be accounted for in the G_{IIC} calculations, for which conclusions based off of Teflon thickness can be made.

Size	Number of Specimens	Avg Fracture Load (N)	Standard Deviation (N)
1	4	443.8	11.5
2	4	713.5	34.76
3	4	1169.8	36.83

Table 3.2: Average fracture loads for sizes 1-3, thin Teflon

3.4 Analysis

3.4.1 LEFM Analysis

From the obtained load-displacement data of the quasi-static tests, one can use Euler Bernoulli Beam theory to obtain the displacement in the ENF beam with respect to the load condition and location in the beam, of which a general form of the equation can be seen in equation (3.1), where v is the beam deflection and q is some distributed load on the beam.

$$\frac{\mathrm{d}^2}{\mathrm{d}x^2}\left(EI\frac{\mathrm{d}^2 v}{\mathrm{d}x^2}\right) = q \tag{3.1}$$

Treating the ENF beam as two pristine beams stacked atop one another, while using boundary conditions of a simply supported beam, the beam equation can be solved for in terms of the geometric dimensions. Solving this equation produces the expression for the displacement of the ENF beam, now incorporating crack length to determine beam

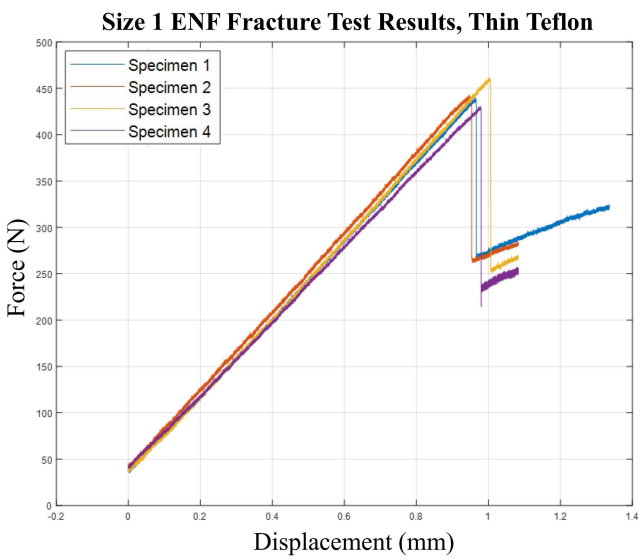

(a) Size 1 Load-Displacement test results

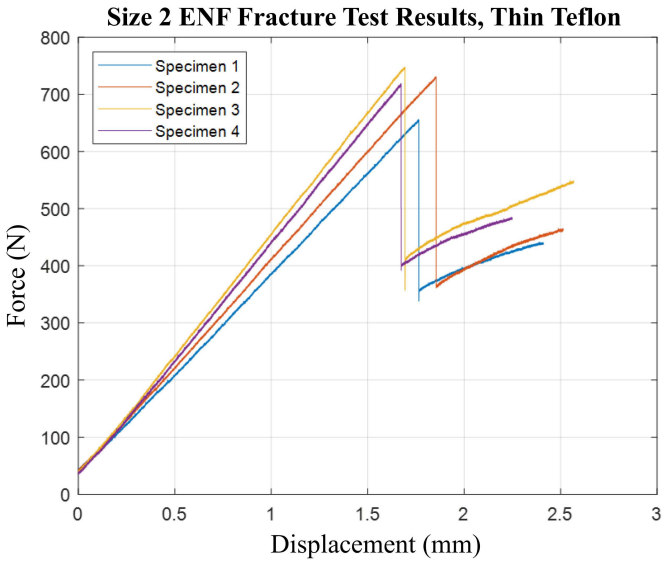

(b) Size 2 Load-Displacement test results

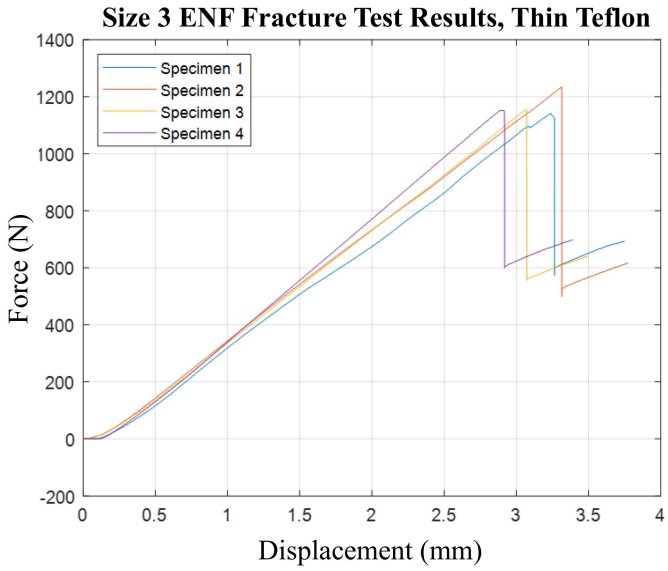

(c) Size 3 Load-Displacement test results

Figure 3.6: Fracture test results of thin Teflon T700 specimens

displacement, seen in equation (3.2). The variables used in equation (3.2) are defined in Figure 3.7.

$$v(L) = \frac{2L^3 + 3a^3}{8Ebh^3} P \tag{3.2}$$

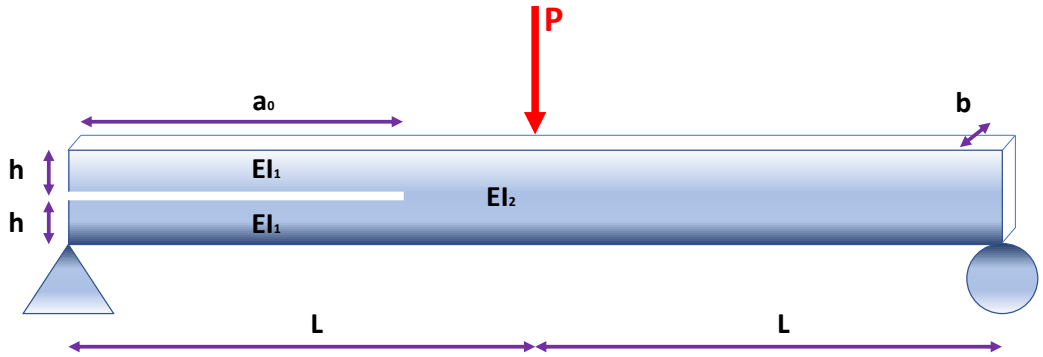

Figure 3.7: Geometric variables used in fracture energy derivation

Although there are different ways to determine G_{IIC}, one can calculate the energy release rate following Irwin's energy approach outlined by Anderson in his textbook *Fracture Mechanics*. Using equation (3.3), the energy available for an increment of crack extension can be measured, where Π is the potential energy supplied by the internal strain energy and external forces [41], [13].

$$G = -\frac{\mathrm{d}\Pi}{\mathrm{d}A} \tag{3.3}$$

Relating this to the energy release rate to the crack growth, the rate of work needed to grow the crack can be related to the area rate of change of crack growth, which indicated crack extension occurs when a critical value is reached, seen in equation (3.4), where w_f is the fracture work per unit surface area.

$$G_c = \frac{\mathrm{d}W_s}{\mathrm{d}A} = 2w_f \tag{3.4}$$

For quasi-static testing, the load is fixed at its loading roller location, the structure is said to be load controlled and therefore can define the potential energy of the beam, and its components as the following:

$$\Pi = U - F \tag{3.5}$$

$$F = P\Delta \tag{3.6}$$

$$U = \int_0^{\Delta} P\Delta = \frac{P\Delta}{2} \tag{3.7}$$

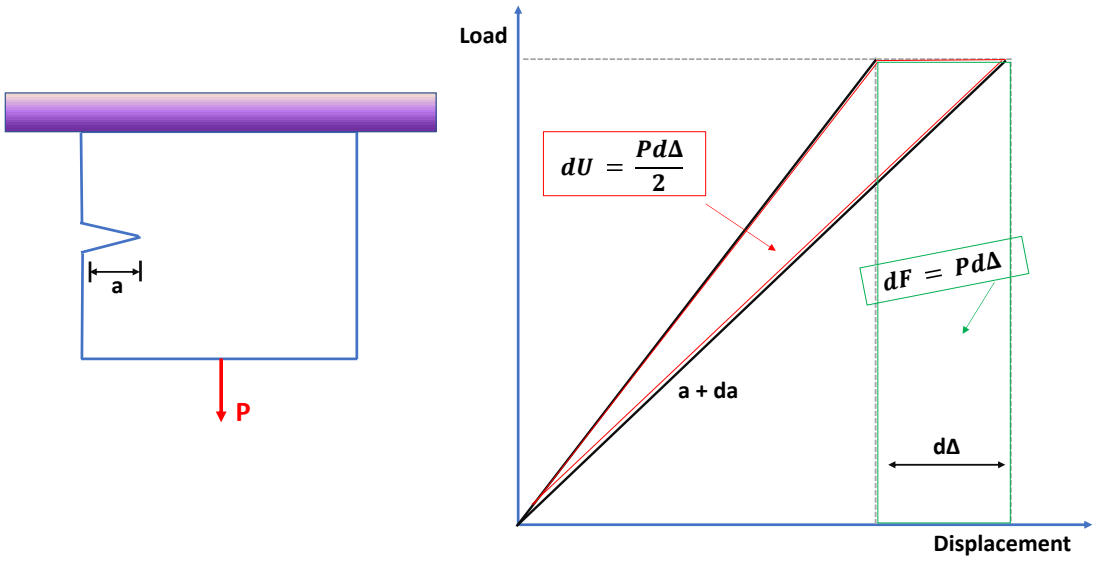

Figure 3.8: Schematic and plot for beam energy equations [13]

where Π is the potential energy, U is the strain energy stored, F is the work done by external forces on the beam, and a is the crack length. Equations (3.5 - 3.7) can be

substituted into equation (3.3) to obtain equation (3.8).

$$G = \frac{1}{b}\left(\frac{\mathrm{d}U}{\mathrm{d}a}\right)_P = \frac{P}{2b}\left(\frac{\mathrm{d}\Delta}{\mathrm{d}a}\right)_P \tag{3.8}$$

Introducing compliance as the inverse of plate stiffness, equation (3.9) can be substituted into (3.8) to obtain G in terms of known variables and their derivatives, equation (3.10).

$$C = \frac{\Delta}{P} = \frac{v(L)}{P} \tag{3.9}$$

$$G = \frac{P^2}{2b}\frac{\mathrm{d}C}{\mathrm{d}a} \tag{3.10}$$

Substituting equations (3.9) and (3.2) into (3.10), one can obtain the full solution for the energy release rate in (3.11).

$$G_{IIC} = \frac{9P^2a^2}{16Eb^2h^3} \tag{3.11}$$

Which is now a function of the specimen geometry and crack length of the ENF specimen.

Results from LEFM analysis can be seen in the color table in Figure 3.9. Note that the LEFM analysis yields multiple values for G_{IIC} which are size dependent, whereas G_{IIC} should be a single value based on material properties. This articulates the inconsistencies with LEFM theory when applied to size affected structures. Because of this and the existence of the non-negligible FPZ that resides at the crack tip, Bažant's Type II SEL must be applied, outlined in the Size Effect Analysis section.

3.4.2 Abaqus Modeling Analysis

In order to account for the non-negligible FPZ and follow the SEL developed by Bažant, Finite Element Analysis (FEA) must be used to augment the experimental results. To describe the energy failure condition at the crack tip, whose mathematics is described in more detail in the next section, the J-integral will be used and can be calculated from FEA corresponding to the energy release rate of the material [53]. Modeling the size 1 specimens using Abaqus explicit modeling with quarter quadratic elements, a model of the

Size	# of Specimens	Thick Teflon Avg Fracture Load (N)	Thick Teflon G_{IIC} (N/mm)	Thin Teflon Avg Fracture Load (N)	Thin Teflon G_{IIC} (N/mm)
1	4	377.6	0.54	443.8	0.52
2	4	615.7	1.01	713.5	0.88
3	4	1159.5	1.32	1169.8	0.92
4	4	1907.9	1.65	N/A	N/A

Figure 3.9: Results from LEFM analysis for both Teflon thicknesses, showing varying G_{IIC} values for different sizes

ENF beam with a designated crack tip and crack seam was defined. Like in experimental 3-point bending tests, an applied displacement was implemented at the beam mid-span, with simply supported beam boundary conditions. Due to the chaotic behavior occurring during crack propagation and extreme mesh sensitivity under mode II loading, the mesh seeds were adjusted at each partition through an iterative process. Modelling the smallest size specimen with 36 mm gauge length, a refined mesh was used with 41950 elements and 128403 nodes using quadratic quadrilateral elements of type CPE8, which can be seen in Figure 3.10.

From this model, calculated J-integral values corresponding to the energy release rate are observed throughout the loading scenario. The J-integral values can be converted to a dimensionless energy release rate, g_α by using equation (3.12).

$$g(\alpha) = \frac{G(\alpha)}{D\sigma_N^2} \tag{3.12}$$

Using three different crack locations of 9.5, 10, 10.5 mm, a linear regression of the dimensionless energy release rate can be plotted to obtain g'_α, seen in Figure 3.11. Then G_f and c_f can be calculated using equation (3.19), where A and C are calculated using a linear regression of the experimental size effect results, seen in Figure 3.12.

Where the size effect regression takes a linear form to identify values for A and C.

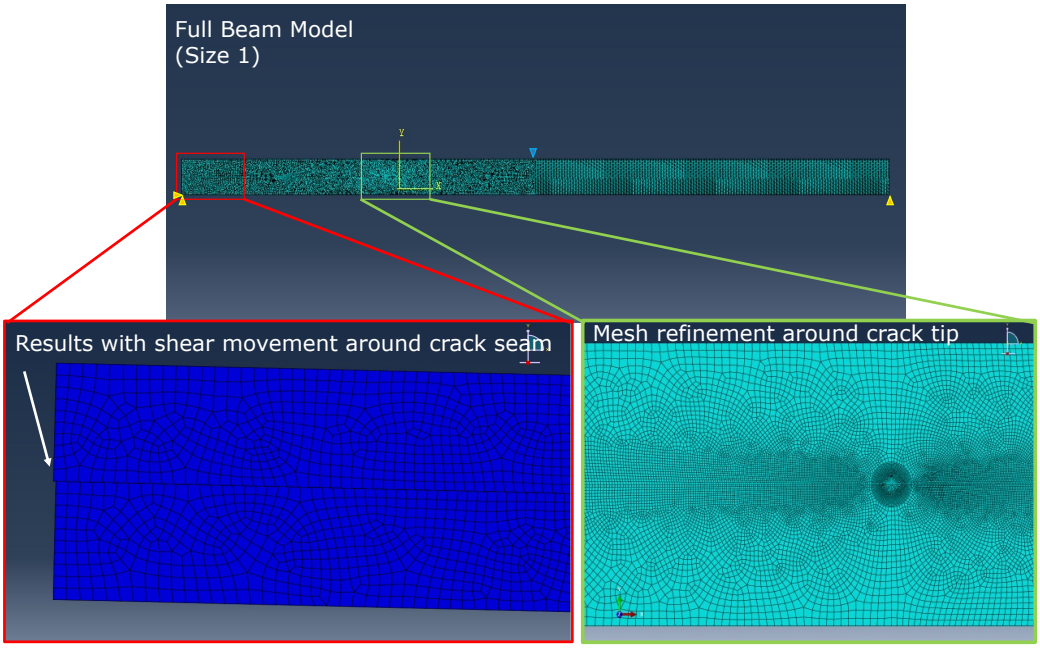

Figure 3.10: Mesh refinement and shear slip movement in Abaqus beam model

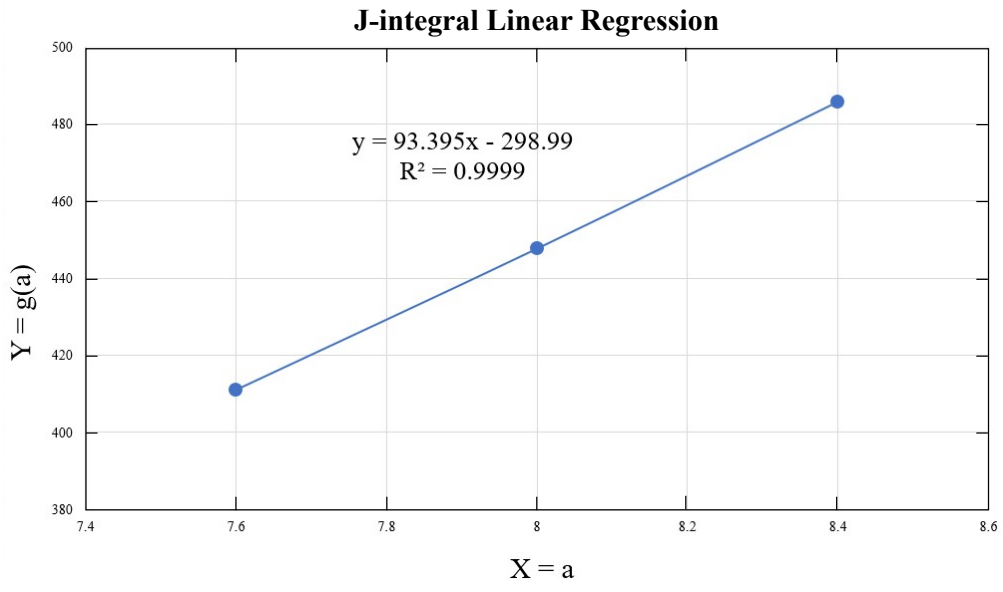

Figure 3.11: Linear regression of J-Integral Abaqus values

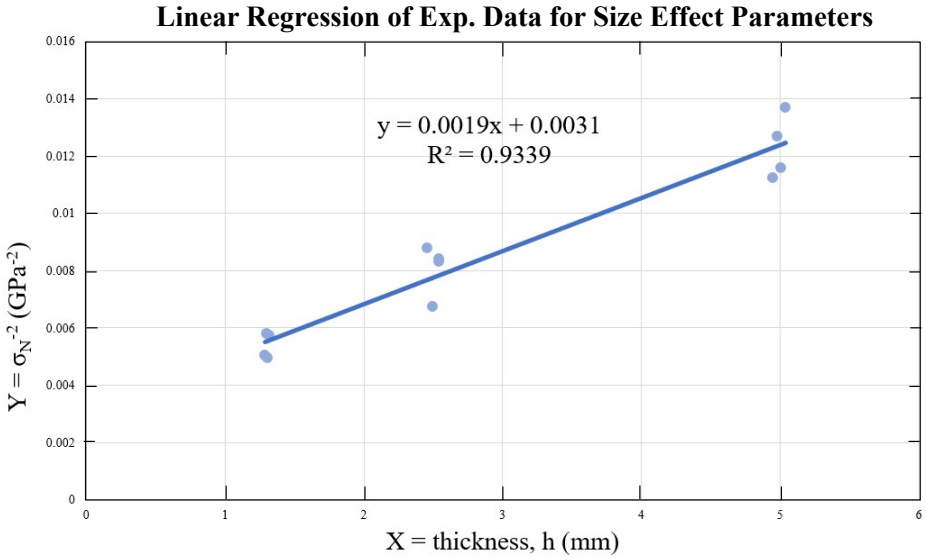

Figure 3.12: Linear regression of experimental size effect values

$$Y = A^{(II)}X + C^{(II)} \tag{3.13}$$

Using the experimental data obtained from the quasi-static size effect tests with FEA data, the fracture energy and associated FPZ size can be calculated from a direct relation of G_f and c_f from the linear regression data, shown in the next section.

3.4.3 Size Effect Analysis

As discussed, it is known that quasi-brittle materials do not behave according to LEFM due to the non-negligible FPZ size and complex fracturing process [**?**, 12, 40, 52, 54, 55]. For this reason, the SEL for mode II interlaminar fracture, formulated by Bažant, must be used to account for the FPZ that exists in the crack tip [52]. Following the derivation of the SEL for mode II fracture, the nominal strength can be represented in (3.14), and later used to identify fracture loads.

$$\sigma_{Nc} = \frac{\sigma_0^{(II)}}{\sqrt{1 + \frac{h}{h_0^{(II)}}}} \tag{3.14}$$

$$\sigma_0 = \sqrt{E * G_f / c_f^{II} g'_{II}(a_0)} \tag{3.15}$$

$$h_0^{II} = c_f^{II} g'_{II}(a_0) / g_{II}(a_0) \tag{3.16}$$

Where σ_{Nc} is the nominal stress, h is a characteristic length, c_f^{II} is the effective FPZ length as a material property, G_f^{II} is the mode II fracture energy, E is the elastic modulus, and $g_{II}(\alpha)$ is the dimensionless energy release rate. Additionally the failure condition that $g'_{II}(\alpha) > 0$ indicates that the structure has positive geometry is assumed. The values for $g_{II}(\alpha)$ and $g'_{II}(\alpha)$ are obtained from Finite Element Analysis (FEA) J-Integral calculation of the model discussed previously. The transformation found in equations (3.17) and (3.18) can be used to convert (3.14) to a linear form, allowing a linear regression to obtain values for the size effect curve, plotted in the previous section in Figure 3.12

$$X = h,\ Y = \sigma_{Nc}^{-2} \tag{3.17}$$

$$\sigma_0^{(II)} = [C^{(II)}]^{1/2},\ h_0^{(i)} = \frac{C^{(i)}}{A^{(i)}} = \frac{1}{A^{(II)}[\sigma_0^{(i)}]^2} \tag{3.18}$$

The stated transformation converts (3.14) to a linear form used as a linear regression of the FEA data which identified values of A and C, which are then used to calculate the fracture energy and associated FPZ size from equations (3.19) and (3.20). Using the experimental data obtained from the quasi-static size effect tests with FEA data stated previously, the fracture energy and associated FPZ size can be calculated using equations (3.19) and (3.20).

$$A = \frac{g(\alpha_0)}{EG_f} \tag{3.19}$$

$$C = \frac{c_f g'(\alpha_0)}{EG_f} \tag{3.20}$$

Where G_f and c_f are the fracture energy and FPZ lengths, respectively. Then the size effect curve can be constructed and the deviation from LEFM is observed in Figure 3.13.

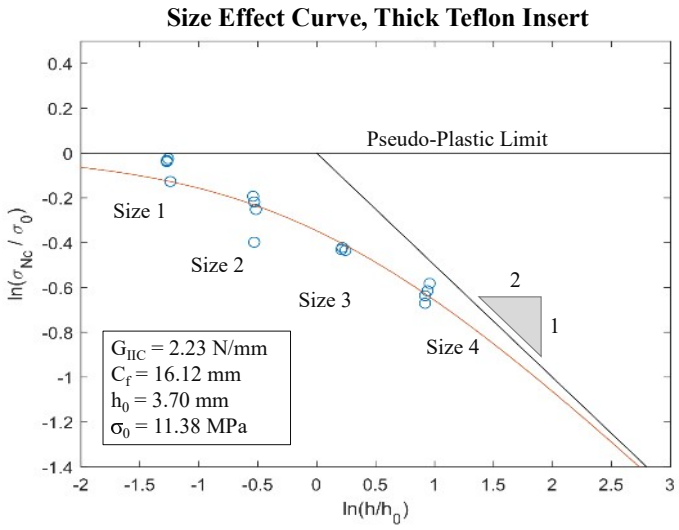

Figure 3.13: Size Effect curve for thick Teflon specimens 1-4

This incorporates the non-negligible FPZ that surrounds the crack tip in the quasi-brittle structures. It is observed that the smaller sized specimens behavior in a more quasi-ductile behavior, trending closer to the pseudo-plastic limit. This supports the findings of Salviato et al. that the damage in the FPZ causes strain redistribution, influencing the structural behavior of the ENF specimens [40]. This close correlation of the test results supports the fact that G_{IIC} acts as a material property, as it is shown to be G_{IIC} =2.23 N/mm for the ENF test specimens manufactured with the thick Teflon insert. The same analysis was conducted on the thinner Teflon specimens (12.5 μm thickness), whose size effect curve can be seen in Figure 3.14.

It is worth noting that the thin Teflon demonstrated lower fracture energy with a G_{IIC} value of 1.48 N/mm, than that of the thicker Teflon. With a thinner Teflon insert, the value for h becomes larger, and from equation (3.11), it is shown that the value for G_{IIC} is highly

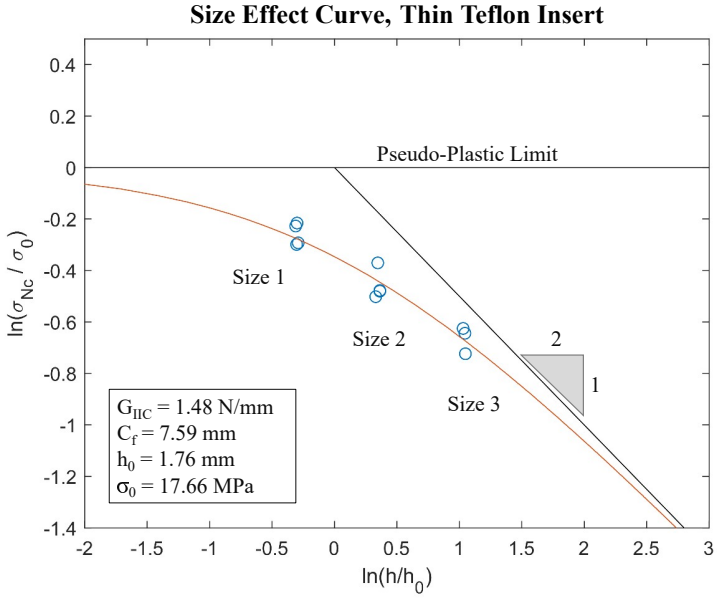

Figure 3.14: Size Effect curve for thin Teflon specimens 1-3

influenced by specimen geometry, specifically h^3, resulting in a lower value of G_{IIC} for larger h.

3.4.4 CZM Formulation

DIC techniques were also employed for both large and small specimens. As discussed previously, smaller sized specimens (sizes 1-2) utilized 2D DIC under microscope, while larger sized specimens (sizes 3-4) utilized 3D DIC with a two-camera pair. This image tracking allows for a full-field strain and crack displacement data to be extracted from the fracture tests, augmenting the load-displacement data obtained from the load frames. Images of an example of the shear strain contour can be seen for one of the size 2 loading examples just before the crack propagates, in Figure 3.15. In these DIC images, the crack location and crack tip can be located, highlighted by the contour gradient that surrounds the Teflon, indicating slipping between the two beam sections. As the loading condition increases, the shear slip increases, as the beam sections continue to displace until the crack grows. This full field

strain data provides insight to the FPZ size that surrounds the crack tip, and aids Finite Element Method (FEM) and CZM modelling to develop a reliable model for future crack growth predictions. These models created from the DIC data are then compared against the experimental data of a variety of specimens demonstrating validity and robustness in the model.

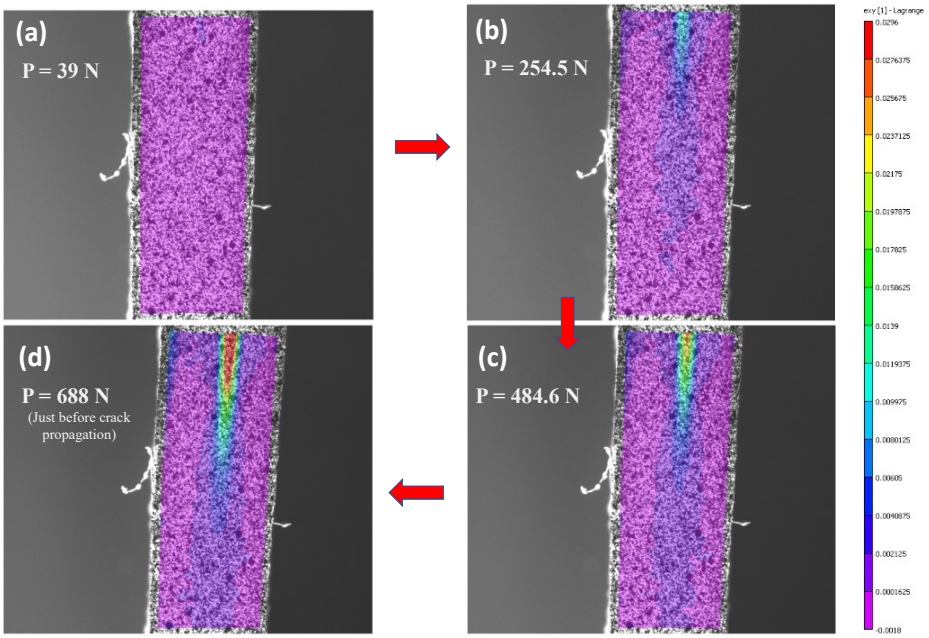

Figure 3.15: Contour gradient from DIC images depicting ϵ_{xy}

Additional research was conducted in tandem by Dr. Han-Gyu Kim using the presented results to formulate and calibrate a mode II CZM using the DIC data obtained from the thin Teflon size effect tests. Shear slip results using the micro-DIC images from the size 1 tests can be seen in Figure 3.18, whose setup is shown in Figure 3.17. This figure analyzes the size 1 in-plane displacement, u, at the peak load. Figure 3.18 identifies the contours of the shear slip that occurs at the precrack and along the predicted crack path.

Separation is clearly observed along this crack path and within the FPZ, denoted by a "zig-zag" shape above and below the predicted crack path. Meanwhile, negligible separation is found outside the precrack and FPZ region, shown with uniform contours above and

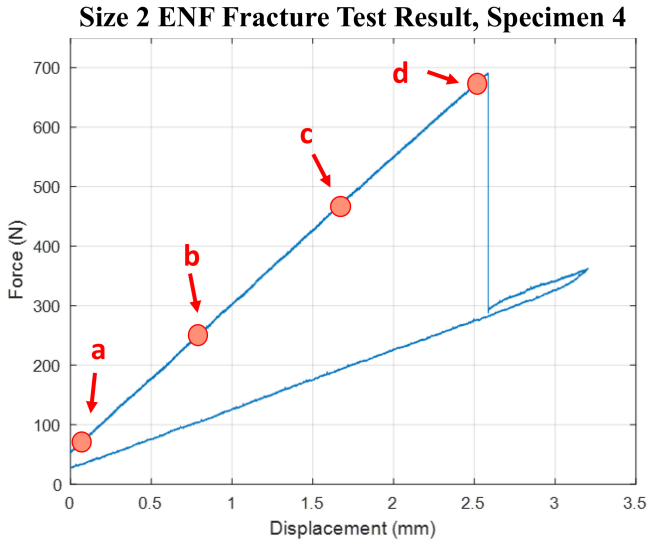

Figure 3.16: Associated load-displacement plot for ϵ_{xy} in Figure 3.15

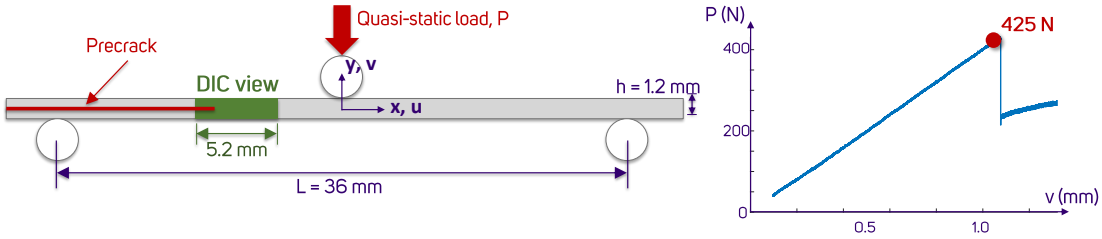

Figure 3.17: Specimen setup referenced in Figure 3.18

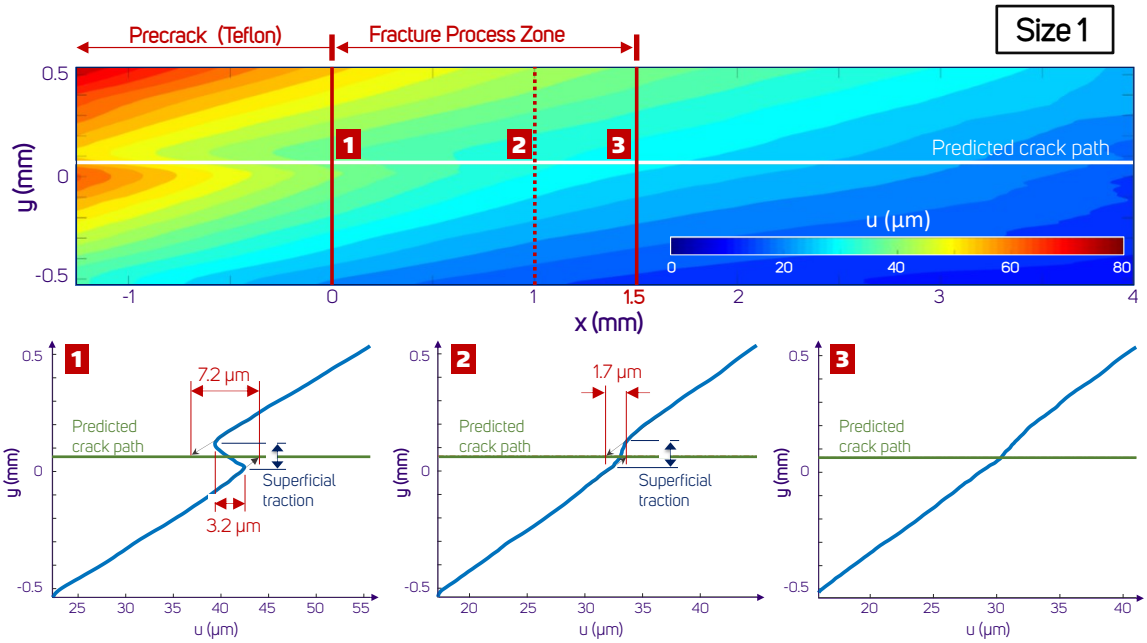

Figure 3.18: Shear slip and FPZ measurement for Size 1, thin Teflon

below the predicted crack path line. These indicate an FPZ size of 1.5 μm for the size 1 specimen. However, shown in part 1 and 2 of Figure 3.18, a superficial traction may have been generated due to the DIC paint speckle. Due to the size effect considerations, it is expected that a nonzero traction exist at the peak load, indicating a partial development of the CZM. Therefore, the actual shear slip at these locations will be some value between the traction-free case (7.2 μm) and the superficial traction case (3.2 μm). Using the fracture data obtained during each size effect test, a mode II CZM can be formulated and calibrated, shown in Figure 3.19, which indicates the CZM development at the crack tip during peak loading for each specimen size denoted by the gold points. This results in a piece-wise softening curve, which will be further validated by comparing shear slip and FPZ size from both simulation and experimentation.

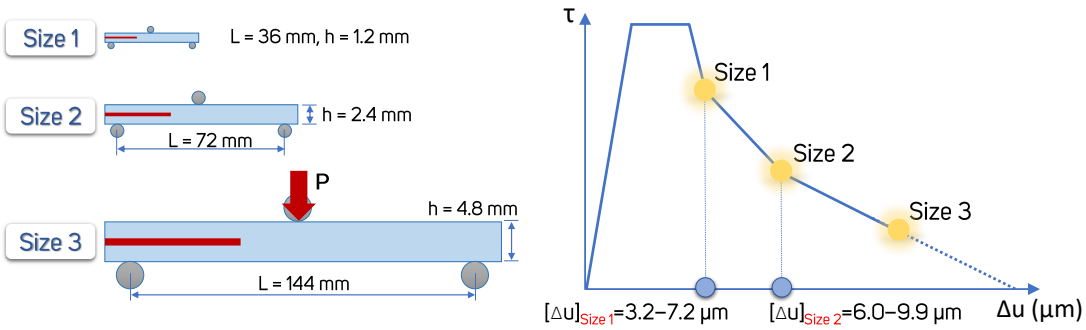

Figure 3.19: Piece-wise CZM formulation for size affected specimens

Chapter 4

MODE II FATIGUE UNDER CONTACT LOADING

4.1 Introduction

This chapter introduces the initial investigatory fatigue tests conducted on carbon/epoxy ENF beam specimens. Using Size 1-3 size effect specimens, a contact fatigue test matrix was created to identify crack growth in ENF specimens under cyclic loading. Load and displacement data from these tests aims to monitor crack growth with respect to loading cycles to construct the Paris Law curve that governs fatigue crack growth. No test matrix exists for ENF specimens undergoing mode II loading. Due to this, a similar procedure was employed using the quasi-static test method articulated in ASTM D7905, those conducted by Al-khudairi et al. for mode II bending fatigue, and based off of the results from within this research [56].

4.2 Experimental Setup

ENF specimens were tested on the Instron fatigue frame in the Mechanical Engineering Test Lab. An image of the test setup, using a similar 3-point bending setup for the larger specimens can be seen in Figure 4.1. Both quasi-static compliance tests and cyclic fatigue tests were conducted on this frame to keep compliance data consistent among tests.

This setup followed the quasi-static test parameters as closely as possible, using a scaled gauge length and initial crack length according to specimen size. The loading and support rollers satisfied the quasi-static ENF standard test method with diameters of 6.32 mm and 7.92 mm, respectively. Using the computer GUI and mechanical controls paired with a 20 kN load cell, test parameters could be input to define load or displacement controlled tests specifying target amplitudes, frequency, and number of cycles. Since this testing was new and not a continuation of previous work, an initial fatigue investigation was required to identify the proper mode II loading parameters to facilitate stable crack propagation, which

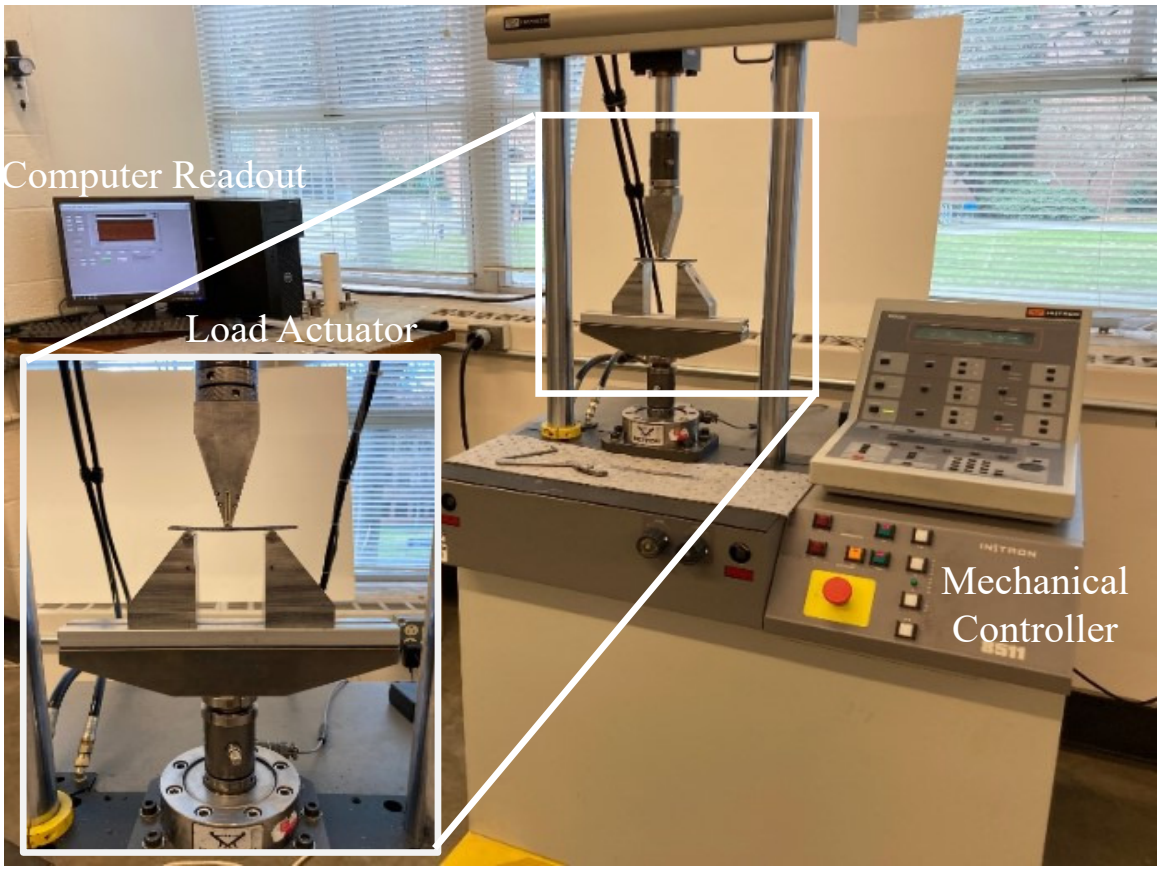

Figure 4.1: MTS fatigue frame in ME lab at UW

was performed using size 2 carbon/epoxy "dummy" specimens of an unknown material type with a thin Teflon insert. A flow chart test matrix for the size 2 dummy specimens was created to achieve the best loading parameters can be seen in Figure 4.2.

The test matrix aimed to conduct both displacement control and load control tests to compare the construction of the Paris Law curve in two directions. Figure 4.3 depicts how this is done. For displacement controlled tests, the load amplitude will reduce as the specimen compliance is increased through crack growth, and hence constructs the Paris Law curve from right to left, eventually approaching the infinite life region where no crack growth will continue to occur at a fixed displacement [36]. Conversely, for load controlled tests,

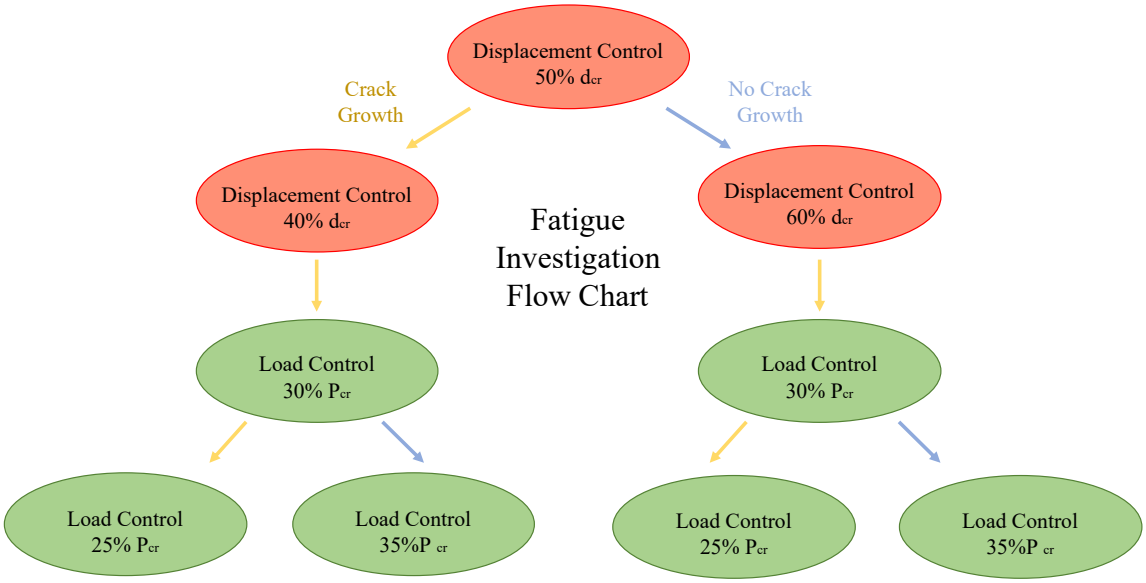

Figure 4.2: Fatigue investigation testing plan flow chart

the displacement amplitude will increase as the specimen compliance changes, approaching Region 3 in the Paris Law curve undergoing rapid crack growth. These initial dummy specimen tests helped identify the fatigue loading required for stable crack growth, while collecting low-noise data. After success with the dummy specimens, the testing moved to the size 1-3 T800 specimens with a thin Teflon insert.

4.3 Test Results

This section will articulate the testing and initial experimental results obtained from both the dummy specimens and the size effect T800 fatigue specimens. Later, in the Analysis section, thorough calculations will be described using the T800 specimen experimental data to construct the Paris law curve.

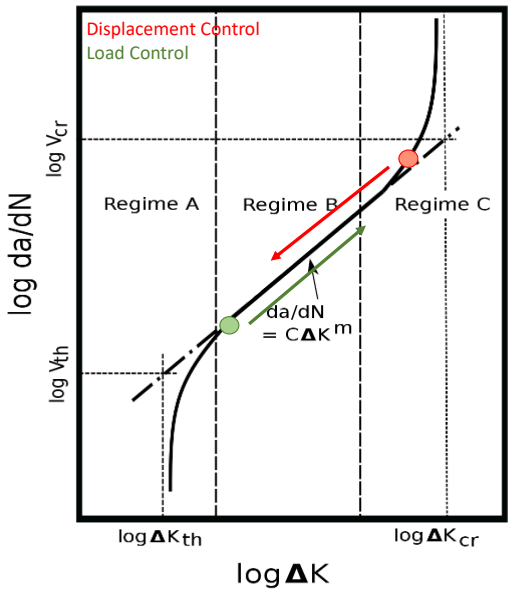

Figure 4.3: Paris curve construction depending on control type

4.3.1 Dummy Specimen Investigation

In order to calculate the crack growth and the Paris Law curve from fatigue test results, initial compliance tests must be conducted on each specimen. These tests were initially conducted on the μTS micro-load frame, similar to those conducted for quasi-static tests, but was later switched to conducting quasi-static compliance tests on the load frame to keep compliance values consistent for each frame. Data was collected for three compliance calibration tests on each size specimen at crack lengths specified in Table 4.1. Initial fracture tests of this material under the same geometric conditions provided critical fracture loading values, which were used to determine the target loading values used in the compliance test, seen in equation (4.1).

$$P_{cc} = P_{cr}\frac{a_0}{a_{cc}} \tag{4.1}$$

Similar to calculations used for quasi-static testing, these compliance test results are used to calculate crack growth using the compliance calibration method, which will be shown in the Analysis section. It was determined that the threshold fatigue region was

Size	$a_1(mm)$	$a_0(mm)$	$a_2(mm)$
1	7	10	13
2	15	20	25
3	30	40	50

Table 4.1: Compliance calibration test crack lengths

better to isolate than the unstable crack growth region of the Paris curve for structural purposes, resulting in displacement controlled tests. Additionally, load control tests often suffered a loss of amplitude control due to the loading roller's inability to provide required displacement at the low, 2 Hz frequency. The results of the size 2 dummy specimen tests displayed a maximum amplitude load between 55-65% of the quasi-static fracture load to yield stable crack growth in <100,000 cycles. The specimens undergoing mode II crack growth were very sensitive to loading, with +-5% of the quasi-static fracture load range at times resulting in infinite life or unstable crack growth. With this loading target and testing information, experimentation moved to the size 1-3 T800 fatigue specimens.

4.3.2 Size 1-3 T800 Fatigue Specimens

In order to identify the peak loading values of the T800 specimens with the thin Teflon insert, fracture tests were conducted, similar to those performed on the T700 specimens in Chapter 3. The average results and dimensions of the T800 fatigue specimens can be seen in Table 4.2. For each specimen, a normalized fracture load was obtained provided the individual specimen geometries, but is not shown here for brevity. With this information, amplitude loading values as a percentage of the fracture load, P_{cr}, could be determined for each specimen size to facilitate crack growth in <100,000 cycles.

Due to a higher ductility in smaller specimens, a slightly higher fatigue loading condition was placed on the size 1 specimen. Following the results made from the size 2 dummy specimens, a displacement controlled fatigue test was conducted with a loading roller displacement corresponding to 65-70% P_{cr}, or an amplitude range of 125 - 440 N. These tests

Size	$P_{cr}(N)$	Width (mm)	Thickness (mm)	Gauge Length (mm)
1	644.16	25.68	1.48	36
2	930.96	24.63	2.78	72
3	1346.44	25.23	5.42	144

Table 4.2: Size 1-3 fracture loads and specimen geometry

are monitored until an asymptotic loading value is reached, indicating an arresting of the crack growth. For these tests, displacement should be constant throughout the duration due to the displacement controlled test.

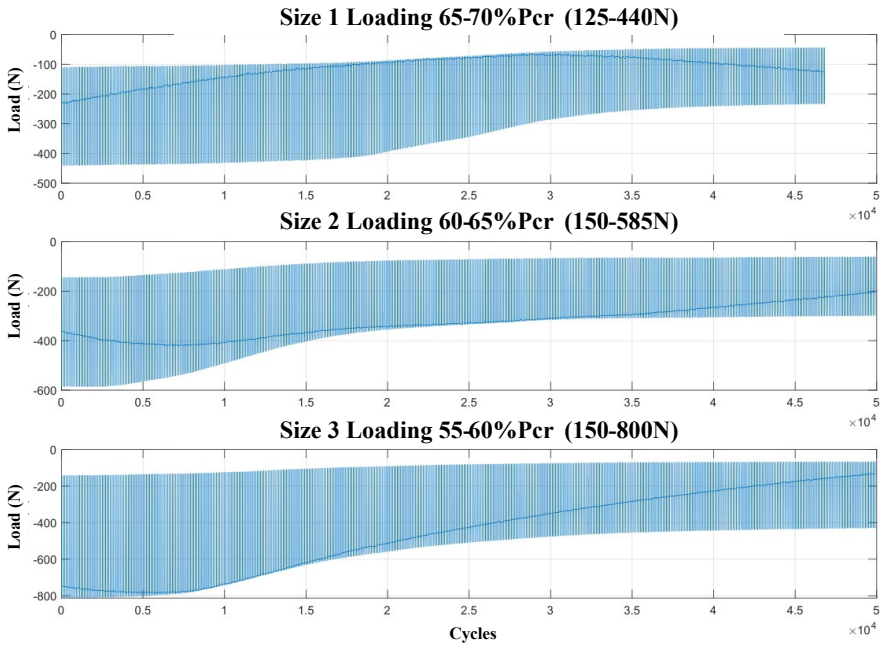

Figure 4.4: Size 1-3 experimental results for load vs. cycle number

Similar behavior is observed with the size 2 specimen. Loading values corresponding to 60-65% P_{cr} resulted in a displacement controlled test with a loading amplitude of 150 - 585 N. In this case, the crack growth occurred much quicker, denoted by a quicker reduction in

load between 0-10,000 cycles. The size 3 specimen had a loading amplitude corresponding to 55-60% P_{cr} of 150 - 800 N, whose behavior is similar to that of the size 2 specimen. These results can be see in Figure 4.4, for each test case. From the experimental data obtained from the size 1-3 specimens, crack lengths and compliance values throughout the load cycle can be calculated. With this information, a Paris Law curve can be formulated for each size, shown in the next section.

4.4 Analysis

The goal of these fatigue tests is to present a Paris Law curve governing fatigue crack growth for each of the size effect specimens. To describe the analysis to obtain the Paris curve from experimental data, first the compliance calibration test results will be presented, then calculation of the crack length and compliance along the loading duration will be shown, and finally the construction of the Paris Law curve will culminate these findings. A developed Matlab script to construct the Paris curve will be uploaded to a group Drive where it can be used in the future.

4.4.1 Compliance Calibration Test Results

Similar to the quasi-static tests, compliance calibration tests were conducted on each specimen at scaled crack length intervals defined in Table 4.1. These must be conducted prior to the fatigue testing to obtain the pristine specimen compliance at the specified crack length to be used in a linear regression to provide compliance values specific to each beam. An example of the size 3 load-displacement plots for the compliance test results can be seen below in Figure 4.5a and 4.5b. The compliance values, A and m, are required to calculate beam compliance and ΔK to construct the Paris Law curve. Size 1-3 compliance values are shown tabulated in Table 4.3

The linear regression takes the form of $C = A + ma^3$, where C is the specimen compliance. A brief derivation follows the compliance calibration method in equation (4.2).

$$\Delta = \frac{2L^3 + 3a^3}{8Ebh^3} P \tag{4.2}$$

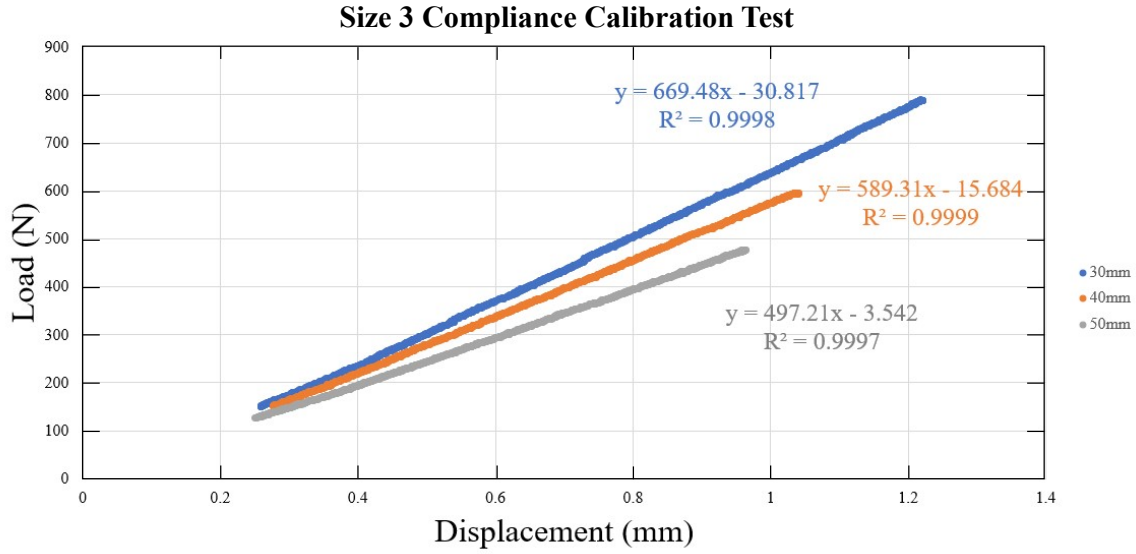

(a) Size 3 compliance calibration test results

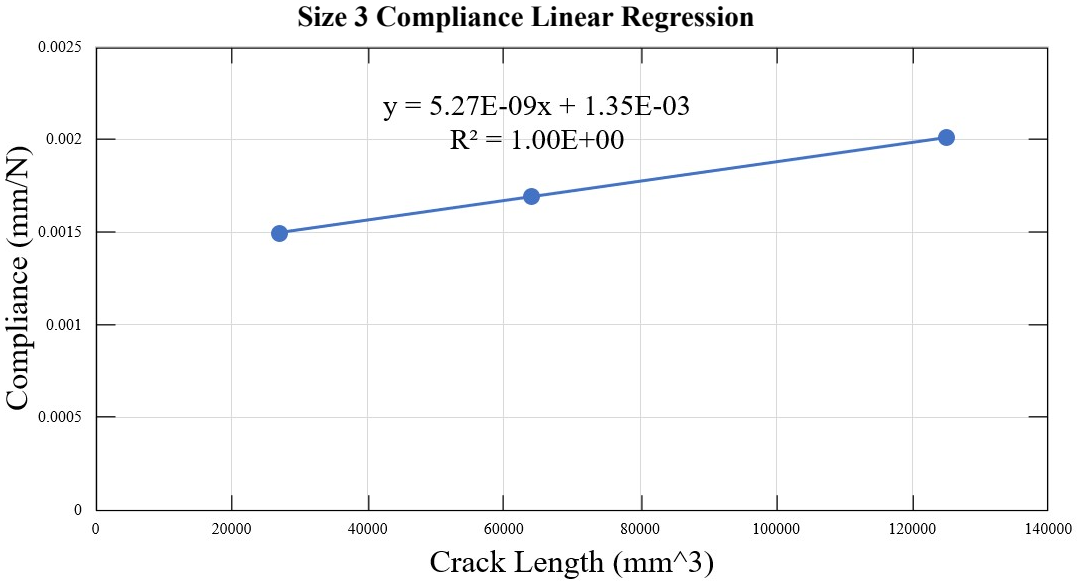

(b) Linear regression of size 3 compliance data

Figure 4.5: Size 3 compliance test results

Size	Crack Length Interval (mm)	A (mm/N)	m ($1/Nmm^2$)
1	7, 10, 13	9.21e-4	2.71e-7
2	15, 20, 25	1.20e-3	4.18e-8
3	40, 50, 60	1.35e-3	5.27e-9

Table 4.3: Size 1-3 compliance values

Where L, B, and h are geometric properties of the specimen, E is the elastic modulus, a is the crack length, and P is the load. Dividing by P, one can obtain compliance shown in equation (4.3).

$$C = \frac{\Delta}{P} = \frac{2L^3 + 3a^3}{8Ebh^3} \tag{4.3}$$

Where equation (4.3) corresponds to the compliance values A and m, of the form seen in equation (4.4).

$$C = A + ma^3 \tag{4.4}$$

4.4.2 Crack Length and Compliance Calculation

Crack length and compliance values can be calculated at every cycle from the experimental data using the values obtained from the compliance calibration tests. Equation (4.4) can be rearranged to solve for crack length at each interval seen in equation (4.5)

$$a_u = (\frac{C_u - A}{m})^{\frac{1}{3}} \tag{4.5}$$

Where C_u can be obtained by the difference in load or displacement, depending on control type. This equation can be seen in equation (4.6).

$$C_u = \frac{d'_{max} - d'_{min}}{P_{max} - P_{min}} \tag{4.6}$$

From the sinusoidal data, these values can be observed at local maxima and minima of the load or displacement curves. A general example of this can be seen in Figure 4.6,

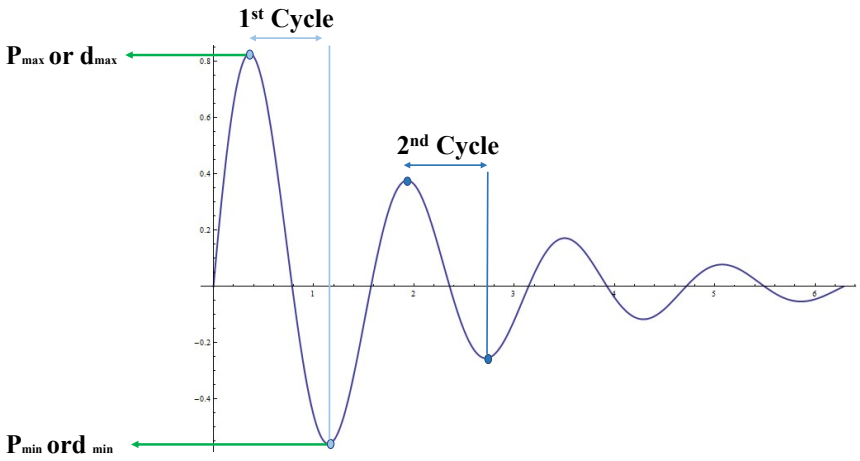

Figure 4.6: Generalized method to calculate fatigue compliance

For load control test, P_{max} and P_{min} should remain constant amplitudes depending on test parameters as these are fixed to influence compliance changes. Conversely, for displacement controlled test, the opposite is true, where displacement values d_{max} and d_{min} should remain the same throughout the test duration. Because these calculations rely heavily on the resolution and consistency of the peak values, it is imperative that a high level of resolution can be obtained from the experimental results.

Applying this to the experimental data, crack length and compliance can be calculated throughout the loading duration. These results can be observed for the three sizes in Figures 4.7 - 4.9.

4.4.3 Paris Curve Construction

Constructing the Paris law, depends on the Stress Intensity Factor, K, and the crack growth rate, da/dN [32]. Paris showed that a power law exists between the stress intensity factor

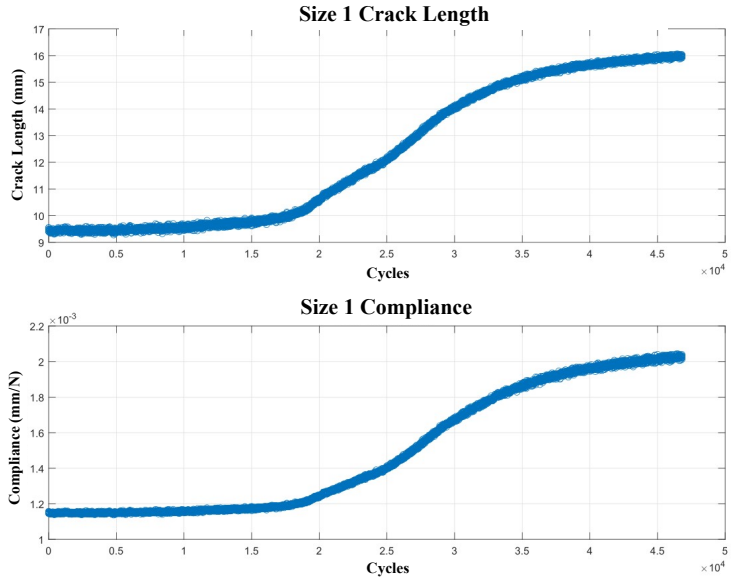

Figure 4.7: Size 1 crack length and compliance values

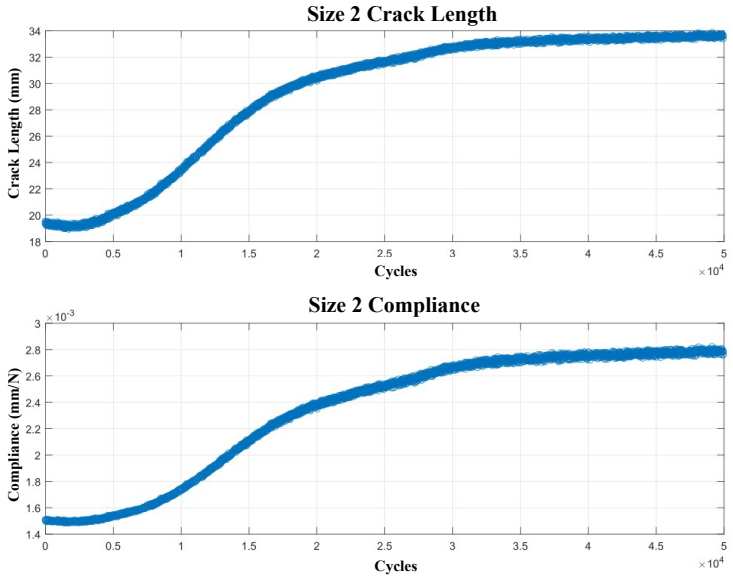

Figure 4.8: Size 2 crack length and compliance values

range, ΔK and crack propagation, taking the form of equation (4.7) [57] [58].

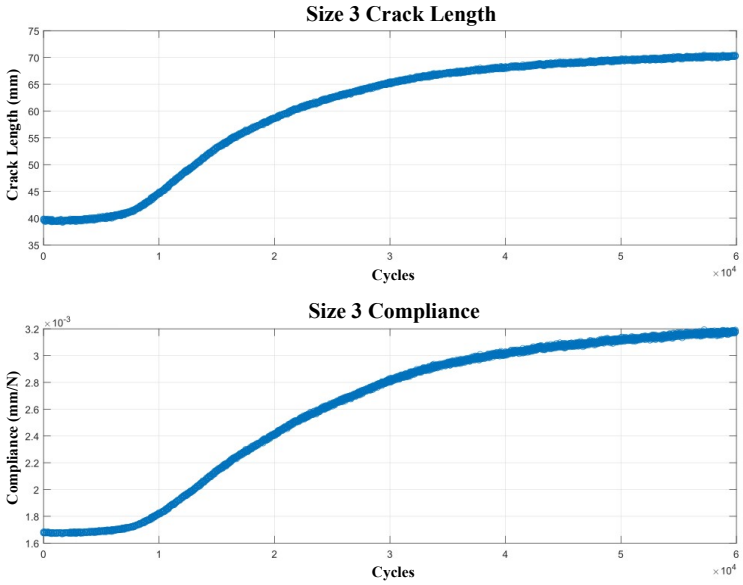

Figure 4.9: Size 3 crack length and compliance values

$$\frac{\mathrm{d}a}{\mathrm{d}N} = C\Delta K_{II}^{m} \tag{4.7}$$

Following LEFM, the mode II Stress Intensity Factor, K, takes the form in equation (4.8).

$$K = \sqrt{E * G_{II}} \tag{4.8}$$

Where from previous derivation it is known that G_{IImax} is defined as is shown in equation (4.9).

$$G_{IImax} = \frac{3mP_{max}^{2}a^{2}}{2B} \tag{4.9}$$

Which when substituted into equation (4.8) becomes the following expression in equation (4.10), where A and m are the compliance values obtained from the compliance calibration tests..

$$K_{IImax} = \sqrt{\frac{3mP_{max}^{2}a^{2}h^{3}}{8AB^{2}h^{3}}} \tag{4.10}$$

Then, ΔK can be calculated as the difference between the maximum and minimum K values, as determined by the cyclical loading condition.

$$\Delta K_{II} = K_{IImax} - K_{IImin} \tag{4.11}$$

To obtain da/dN, an equation must be fit to the experimental data for crack length as a function of cycle number, a(N). To do so, a 4th order fit was used on a section of the crack length data to provide a good fit correlation, $R^2 > 0.99$. The results of these fit equations for each size are shown in Figure 4.10a - 4.10c. It was found that the slope of the stable crack growth region of the Paris Curve is highly sensitive to the curve fit equations. For this reason, the crack growth equations were chosen starting with the linear region of crack growth for the best polynomial fit.

Using the 4th order polynomial fit functions, the first derivative can be taken with respect to the number of cycles. Evaluating da/dN at each cycle provides the rate of change of crack growth, which can be plotted against the stress intensity factor, ΔK. These results can be found in Figure 4.11.

Since these tests were conducted using displacement control, only regions A and B were constructed. These regions correspond to infinite fatigue life (region A, denoted by a more vertical region of the curve) and stable crack growth (region B, denoted by a linear region of the curve). These results show both an increasing ΔK and an increasing linear slope for larger size specimens. This corroborates the findings of Guo et al. who identified Paris curves for mode I fracture in epoxy. Their results displayed an increasing linear slope for larger size specimens, as is found in these results [37]. This recommends that in addition to quasi-static testing, the non-negligible FPZ affects the physics surrounding crack propagation under fatigue loading. Figure 4.11 denotes the discrepancies between the slope of the linear stable crack growth region and the fatigue threshold values, caused by the presence of the non-negligible FPZ that surrounds the crack tip.

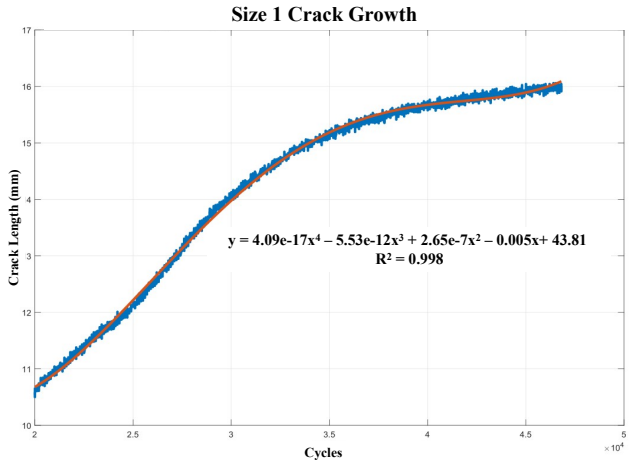

(a) Size 1 crack growth fit equation results

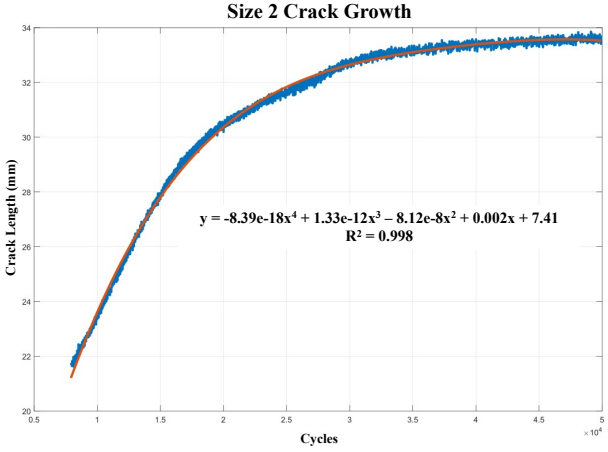

(b) Size 2 crack growth fit equation

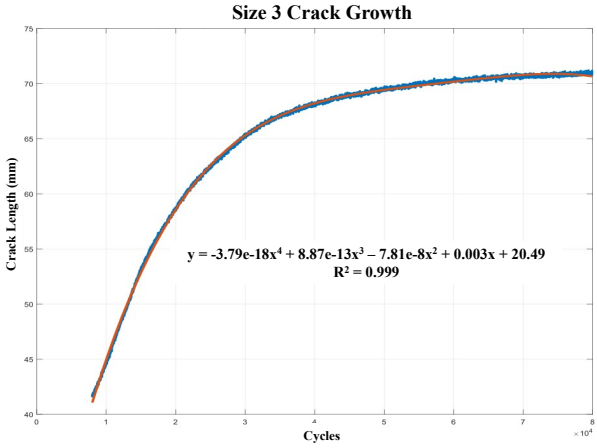

(c) Size 3 crack growth fit equation

Figure 4.10: Size 1-3 crack growth fit equations

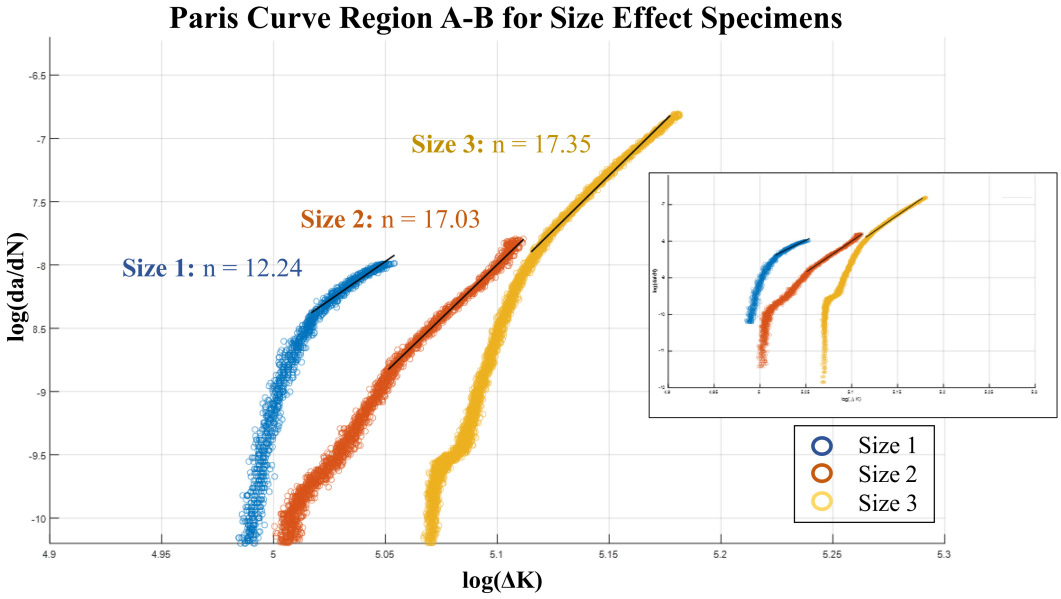

Figure 4.11: Constructed Paris curve with size 1-3 specimens

4.5 Future Work

Future work is planned for both quasi-static fatigue and forced-dynamic fatigue, which will be discussed here. These tests aim to create repeatable results for size affected fatigue specimens for both test types.

4.5.1 Quasi-Static Fatigue

Additional tests are designed to conduct fatigue cycles in a load-controlled setting to augment the results of the presented displacement-controlled tests. These would enable a Paris Curve construction from right to left, creating regions B and C for stable and unstable crack growth. These results will be merged with the currently presented displacement-controlled results to create a full representation of the fatigue Paris Curve for the size effect specimens. These tests are tentatively planned for May 2021.

4.5.2 Forced-Dynamic Fatigue

Although not tested in this research, size effect specimens were prepared for forced-dynamic fatigue to be tested at Wright-Patterson AFB. These tests are still planned to follow the initial calculations made in Chapter 2 to investigate crack growth in a forced-dynamic fatigue setting using various buckled rises. These tests serve an investigatory purpose, but require a shaker table capable of high-G loading, which is not available at the UW. Due to this, these tests could not be completed in-house.

Chapter 5

CONCLUSION

Quasi-Static size effect tests and fatigue tests were conducted on carbon/epoxy beam specimens to identify mode II fracture characteristics and advance CZM development of these materials. Additionally, material properties such as G_{IIC} and C_f were calculated to identify the influence of varying Teflon thickness that create the specimen precrack. The following conclusions are worth noting:

- Size effect testing for four different sizes of carbon/epoxy beam specimens observed excellent agreement to Bažant's SEL, to include smaller sizes found past the deviation of LEFM into the Pseudo-Plastic limit. This further emphasizes the importance of accounting for the non-negligible FPZ size in smaller sized structures.

- Teflon thickness influences material properties of G_{IIC} and C_f, finding thicker tested Teflon yielded values of $G_{IIC} = 2.23$ N/mm and $C_f = 16.12$ mm, while thinner Teflon showed $G_{IIC} = 1.48$ N/mm and $C_f = 7.59$ mm. This recommends utilizing the thinnest Teflon insert available to reduce the Teflon thickness influence.

- Tests and data collected from this research aids CZM development performed in tandem to this research, recommending an accurate CZM for this material must contain a piece-wise shape to accurately model pre, and post-peak behavior for size affected structures. This incorporates a plasticity plateau to account for ductile behavior found around the crack tip and smaller specimens.

- Initial fatigue tests on the T800S carbon/epoxy beams with a thin Teflon insert identify the FPZ influence with size affected Paris curves. Due to specimen sizing and FPZ influence, threshold values and linear slope values for stable crack growth vary with respect to structure size.

This experimental investigation creates a robust testing program to identify mode II fracture and fatigue characteristics under size effect influence. Information from these and future tests are imperative to characterizing damage that can become present and grow under high stress states like those encountered with modern day flight vehicles in supersonic and hypersonic flight regimes. These materials are already being used and employed in these industries, making damage prediction and modelling from empirical results a necessity to ensure safe operation of aged aircraft and equipment.

Bibliography

[1] D. Gay, S. Hoa, and S. Tsai. *Composite Materials: Design and Applications.* CRC Press, 2003.

[2] Sampe. Advanced Composites Advance U.S. Air Force Aviation, 2019. Accessed: 2021-01-20. https://www.nasampe.org/page/MilitaryAircraft.

[3] N. Zazulia. Rejuvenating the Raptor: Roadmap for F-22 Modernization, 2018. Accessed: 2021-01-20. https://www.aviationtoday.com/2018/10/11/rejuvenating-raptor-roadmap-f-22-modernization/.

[4] D. Miracle and S. Donaldson. *ASM Handbook: Composites*, volume 21. American Society for Metals, 2001.

[5] Boeing. Boeing 787 By Design: Advanced Composite Use, 2020. Accessed: 2021-01-20. https://www.boeing.com/commercial/787/by-design//advanced-composite-use.

[6] J. Sloan. Composites World: Skinning the F-35 Fighter, 2009. Accessed: 2021-01-20. https://www.compositesworld.com/articles/skinning-the-f-35-fighter.

[7] Y. Sun and H. Smith. Review and Prospect of Supersonic Business Jet Design. *Elsevier*, 2016.

[8] H. Kim and R. Wiebe. Numerical Investigation of Stress States in Buckled Laminated Composite Plates Under Dynamic Loading. 2019.

[9] N. Zimmerman and P. Wang. A Review of Failure Modes and Fracture Analysis of Aircraft Composite Materials. *Elsevier*, 2020.

[10] Z. Bažant and J. Planas. Fracture and Size Effect in Concrete and Other Quasibrittle Materials. 16, 1997.

[11] Z. Bažant. Scaling Theory for Quasibrittle Structural Failure. *National Academy of Sciences*, 101, 2004.

[12] M. Salviato, K. Kirane, S. Ashari, Z. Bažant, and G. Cusatis. Experimental and Numerical Investigation of Intra-Laminar Energy Dissipation and Size Effect in Two-Dimensional Textile Composites. *Composites Science and Technology*, 135:67–75, 2016.

[13] T. Anderson. *Fracture Mechanics: Fundamentals and Applications*. Taylor and Francis Group, 3rd edition, 2005.

[14] S. Burtscher, B. Chiaia, K. Willam, J. Dempsey, G. Ferro, V. Gopalaratnam, P. Prat, K. Rokugo, V. Saouma, V. Slowik, and L. Vitek. Quasibrittle Fracture Scaling and Size Effect: Final Report. *Materials and Structures*, 37(272):547–568, 2004.

[15] W. Li, Y. Qiao, J. Fenner, K. Warren, M. Salviato, Z. Bažant, and G. Cusatis. Elastic and Fracture Behavior of Three-Dimensional Ply-to-Ply Angle Interlock Woven Composites: Through-Thickness, Size Effect, and Multiaxial Tests. *Composites Part C: Open Access*, 4, 2021.

[16] M. Salviato, S. Ashari, and G. Cusatis. Spectral Stiffness Microplane Model for Damage and Fracture of Textile Composites. *Composite Structures*, 137, 2016.

[17] K. Kirane, M. Salviato, and Z. Bažant. Microplane-Triad Model for Elastic and Fracturing Behavior of Woven Composites. *Journal of Applied Mechanics*, 83, 2016.

[18] M. Salviato, V. Chau, L. Weixin, Z. Bažant, and G. Cusatis. Direct Testing of Gradual Postpeak Softening of Fracture Specimens of Fiber Composites Stabilized by Enhances Grip Stiffness and Mass. *Journal of Applied Mechanics*, 83, 2016.

[19] C. Ceccato, M. Salviato, C. Pellegrino, and G. Cusatis. Simulation of Concrete Failure and Fiber Reinforced Polymer Fracture in Confined Columns with Different Cross Sectional Shape. *International Journal of Solids and Structures*, 108, 2017.

[20] C. Mefford, Y. Qiao, and M. Salviato. Failure Behavior and Scaling of Graphene Nanocomposites. *Composite Structures*, 176, 2017.

[21] Y. Qiao and M. Salviato. Strength and Cohesive Behavior of Thermoset Polymers at the Microscale: A Size-Effect Study. *Engineering Fracture Mechanics*, 213, 2019.

[22] Y. Qiao and M. Salviato. Study of the Fracturing Behavior of Thermoset Polymer Nanocomposites via Cohesive Zone Modeling. *Composite Structures*, 220, 2019.

[23] S. Ko, J. Yang, M. Tuttle, and M. Salviato. Effect of the Platelet Size on the Fracturing Behavior and Size Effect of Discontinuous Fiber Composite Structures. *Composite Structures*, 227, 2019.

[24] S. Ko, J. Davey, S. Douglass, J. Yang, M. Tuttle, and M. Salviato. Effect of the Thickness on the Fracturing Behavior of Discontinuous Fiber Composite Structures. *Composites Part A: Applied Science and Manufacturing*, 125, 2019.

[25] S. Ko, K. Chan, R. Hawkins, R. Jayaram, C. Lynch, R. El Mamoune, M. Nguyen, N. Pekhotin, N. Stokes, D. Wu, and J. Yang. Experimental and Numerical Characterization of the Intra-Laminar Fracturing Behavior in Discontinuous Fiber Composite Structures. 2018.

[26] W. Li, C. Jin, M. Salviato, and G. Cusatis. Modeling of Failure Behavior of Anisotropic Shale Using Lattice Discrete Particle Model. 2015.

[27] W. Li, Z. Jin, and G. Cusatis. Size Effect Analysis for the Characterization of Marcellus Shale Quasi-brittle Fracture Properties. *Rock Mechanics and Rock Engineering*, 52, 2019.

[28] Z. Bažant and Q. Yu. Universal Size Effect Law and Effect of Crack Depth on Quasi-Brittle Structure Strength. *Journal of Engineering Mechanics*, 2009.

[29] C. Sun and Z. Jin. *Fracture Mechanics Chapter 9: Cohesive Zone Model.* Academic Press, 2012.

[30] G. Barenblatt. The Mathematical Theory of Equilibrium Cracks in Brittle Fracture. *Advances in Applied Mechanics*, 7, 1962.

[31] A. Deleo and M. Salviato. Computational Study for Size Effect in Composites and Nanocomposites. *AIAA*, 2018.

[32] P. Paris, M. Gomez, and W. Anderson. A Rational Analytic Theory of Fatigue. *The Trend in Engineering*, 1961.

[33] P. Paris and F. Erdogan. A Critical Analysis of Crack Propagation Laws. *Journal of Fluids Engineering*, 85, 1963.

[34] N. Pugno, M. Ciavarella, P. Cornetti, and A. Carpinteri. A Generalized Paris' Law for Fatigue Crack Growth. *Journal of Mechanics and Physics of Solids*, 2005.

[35] D. Roylance. Fatigue. *Massachusetts Institute of Technology Department of Materials Science and Engineering*, 2003.

[36] A. Ekberg. Fatigue Crack Propagation. *Chalmers Solid Mechanics*, 1997.

[37] K. Guo, Y. Qiao, and M. Salviato. Scaling of Fatigue Crack Growth in Pristine Epoxy. *American Society for Composites*, 2018.

[38] K. Tidwell. Investigating the Fracture Behavior and Damage Mechanisms of Discontinuous Fiber Composites Under Significant Out-Of-Plane Loading. 2020.

[39] J. Teixeira, R. Campilho, and F. da Silva. Numerical Assessment of the Double-Cantilever Beam and Tapered Double-Cantilever Beam Tests for the GIC Determination of Adhesive Layers. *The Journal of Adhesion*, 94, 2018.

[40] M. Salviato, K. Kirane, Z. Bažant, and G. Cusatis. Mode I and II Interlaminar Fracture in Laminated Composites: A Size Effect Study. *Journal of Applied Mechanics*, 2019.

[41] F. Marcelo and S. de Moura. Interlaminar Mode II Fracture Characterization. *Portuguese Foundation for Science and Technology*, 2004.

[42] ASTM International. *D7905: Standard Test Method for Determination of the Mode II Interlaminar Fracture Toughness of Unidirectional Fiber-Reinforced Polymer Matrix Composites*, 2014.

[43] M. Ayatollahi, A. Ajdani, A. Akhavan-Safar, and L. da Silva. Effect of Notch Length and Pre-Crack Size on Mode II Fracture Energy of Brittle Adhesives. *Engineering Fracture Mechanics*, 2019.

[44] G. Murri and R. Martin. Effect of Initial Delamination on Mode I and Mode II Interlaminar Fracture Toughness and Fatigue Fracture Threshold. *Composite Materials: Fatigue and Fracture*, 4:239–256, 1993.

[45] N. Shivakumar, R. Panduranga, J. Skujins, and S. Miller. Assessment of Mode-II Fracture Tests for Unidirectional Fiber Reinforced Composite Laminates. *Journal of Reinforced Plastics and Composites*, 34(23):1905–1925, 2015.

[46] Y. Qiao and M. Salviato. Study of the Fracturing Behavior of Thermoset Polymer Nanocomposites Via Cohesive Zone Modeling. *Composite Structures*, 220:127–147, 2019.

[47] K. Kirane and Z. Bažant. Size Effect in Paris Law and Fatigue Lifetimes for Quasibrittle Materials: Modified Theory, Experiments and Micro-Modeling. *International Journal of Fatigue*, 2015.

[48] ASTM International. *ASTM D5687: Standard Guide for Preparation of Flat Composite Panels with Processing Guidelines for Specimen Preparation*, 2020.

[49] R. Geerts. EpoxyWorks: Vacuum Bagging Basics, 2019. Accessed: 2021-01-19. https://www.epoxyworks.com/index.php/vacuum-bagging-basics/.

[50] Toray Composites (America) Inc. Procedures for Agate Prepreg Materials Laminate Properties. 2002.

[51] F. Moroni A. Zucchelli A. Pirondi G. Giuliese, R Palazzetti. Cohesive Zone Modelling of Delamination Response of a Composite Laminate with Interleaved Nylon 6,6 Nanofibers. *Composites. Part B, Engineering*, 78:384–392, 2015.

[52] Z. Bažant M. Salviato, K. Kirane and G. Cusatis. Mode I and II Interlaminar Failure in Laminated Composites: A Size Effect Study. *Journal of Applied Mechanics*, 2019.

[53] J. Rice. A Path Independent Integral and the Approximate Analysis of Strain Concentration by Notches and Cracks. *Journal of Applied Mechanics*, 35, 1968.

[54] C. Carloni, G. Cusatis, M. Salviato, J. Le, C. Hoover, and Z. Bažant. Critical Comparison of the Boundary Effect Model with Cohesive Crack Model and Size Effect Law. *Engineering Fracture Mechanics*, 215:193–210, 2019.

[55] G. Cusatis and E. Schauffert. Cohesive Crack Analysis of Size Effect. *Engineering Fracture Mechanics*, 76:2163–2173, 2009.

[56] O. Al-Khudairi, H. Hadavinia, A. Waggott, E. Lewis, and C. Little. Characterizing Mode I/Mode II Fatigue Delamination Growth in Unidirectional Fibre Reinforced Polymer Laminates. *Materials and Design*, 2014.

[57] A. Carpinteri and F. Montagnoli. Scaling and Fractality in Subcritical Fatigue Crack Growth: Crack-Size Effects on Paris' Law and Fatigue Threshold. *Fatigue and Fracture of Engineering Materials and Structures*, 2019.

[58] L. Anand and D. Parks. Fatigue Crack Propagation Supplementary Notes. *Massachusetts Institute of Technology Department of Mechanical Engineering Cambridge, Massachusetts 02139*, 2004.